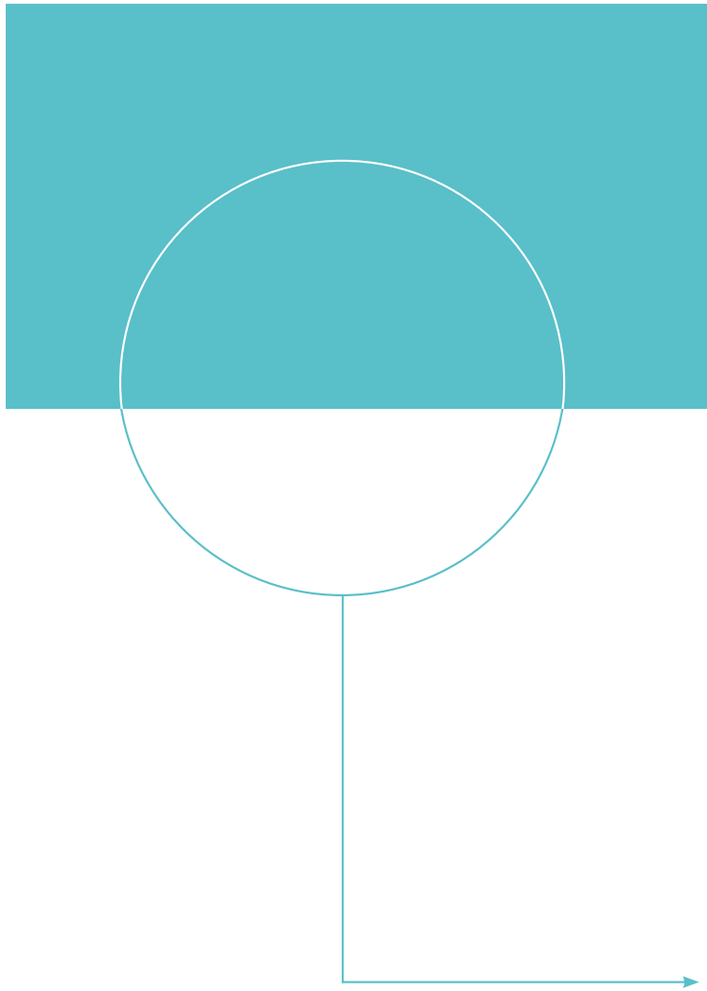

Master's thesis

2021

Elena Medori

NTNU
Norwegian University of
Science and Technology
Faculty of Engineering
Department of Mechanical and Industrial Engineering

Elena Medori

Mechanical Behavior of FDM printed lattice structures with potential for Biomedical Application

June 2021

NTNU
Norwegian University of
Science and Technology

NTNU
Norwegian University of
Science and Technology

NTNU
Norwegian University of
Science and Technology

Mechanical Behavior of FDM printed lattice structures with potential for Biomedical Application

Elena Medori

Submission date: June 2021
Supervisor: Filippo Berto
Co-supervisor: Seyed Mohammed Javad Razavi

Norwegian University of Science and Technology
Department of Mechanical and Industrial Engineering

Abstract

The following work took place in Trondheim, at the Norwegian University of Science and Technology (NTNU), due to the uniqueness of the equipment present in NTNU for the production of samples with Fluid Deposition Model and for their characterization at different scale in the presence of multiaxial loads and mixed modes. The aim of the work is studying the mechanical behavior of produced lattice structures through mechanical testing in order to reveal information about the material's properties under dynamic or static forces. This because the global medical device market has gone through remarkable developments and advancements proposing excellent ways to repair or replace lost tissues and damaged organs of the human body, such as bone, skin or cartilage thanks to designed lattice structures as scaffolds. For these purposes, it is of fundamental importance to understand the optimal design of such scaffolds and their mechanical properties. Indeed, it is desirable for the scaffolds to have mechanical properties close to those of the native tissue or organ, and to be able to avoid "possible side effects" resulting from the stress-shielding mechanism. According to the recent research studies in the literature, there is high dependency of the scale and thickness effect on the mechanical properties of conventionally designed parts produced via additive manufacturing. The significance of the scale effect and the wall thickness effect on the mechanical properties is still to be investigated. For these reasons, first cubic test specimens are designed and divided into three categories with the dimensional constraints of keeping constant porosity, constant wall thickness, and constant cubic size. Then a total number of 30 sheet-based TPMS gyroid lattices are fabricated from PLA (Polylactic Acid) via FDM technique. The fabricated parts are then subjected to mechanical loading to evaluate their energy absorption and mechanical strength. High-resolution images are captured in order to monitor the compression behavior during the tests. Finally, the experimental results from compression tests are compared and the systematic dependency of the mechanical behavior to the wall thickness and scale is discussed.

TABLE OF CONTENTS

Chapter 1: Introduction

In order to have clear the key concepts of this project a relatively broad range of theory is needed. This chapter presents the fundamental theory behind lattice structures in general and proceeds more in-depth with TPMS and gyroids. Especially gyroid structures, their relevant mathematical equations and mechanical properties are presented since this could be considered the core of theory behind this project. A general explanation of linear FEA and DIC is also presented to provide the necessary understanding of calculations and analysis that are made. This is anticipated by an introduction to additive manufacturing, 3D-printing Fluid Deposition Model, general mechanical values of a material and general characteristic of human bone.

1.1) 3D printing

3-D printing, also referred to as additive manufacturing (AM), is a technique for fabricating a wide range of structures and complex geometries from three-dimensional (3D) model data. The process consists of printing successive layers of materials that are formed on top of each other. This technology has been developed by Charles Hull in 1986 in a process known as stereolithography (SLA). 3D-printing, which involves various methods, materials and equipment, has evolved over the years and could transform manufacturing and logistics processes [1].

The 3D printing technology has been in use more than three decades in the automobile and aeronautical industries. In the medical field, the use of this technology was limited only to 3D printing of anatomical models for educational training purposes. Only with the recent advancements in developing novel biodegradable materials has the use of 3D printing in medical and pharmaceutical fields boomed. Today, additive manufacturing technology has wide applications in the clinical field and is rapidly expanding. It has revolutionized the healthcare system by customizing implants and prostheses, building biomedical models and surgical aids personalized to the patient, bioprinting tissues and living scaffolds for regenerative medicine. Table 1 shows the applications of 3D printing technology in various sectors.

SECTOR	APPLICATIONS
Industry	Jings, fixtures, and end-use parts for aeronautical industry. Prototypes and spare parts for automotive industry.
Medical	Surgical models for perioperative surgical preparations. Dental fixtures, bridges, and crowns. Customized patient specific implants and prostheses. Living tissue scaffolds for tissue engineering and regenerative medicine.
Pharmaceutical	Customized implants for drug delivery. Tablets, capsules, and other patient specific design.
Food	Designing and 3D printing complex shaped cakes, cookies, candies, pizzas and other desserts.
Fashion	Jewelry, clothes, shoes, and other accessories.
Household	Plates, cups, spoons, holders, and other common household objects.
Miscellaneous	Space: building prototypes and parts in space. Chemical industry: fabricating complex molecules and compounds. Construction: scale models with intricate architectures.

Table 1: Application of 3D printing technology in various sectors [2].

Like any manufacturing process, 3D printing needs high quality materials that meet consistent specifications to build consistent high-quality devices. To ensure this, procedures, requirements, and agreements of material controls are established between the suppliers, purchasers, and end-users of the material. 3D printing technology is capable to produce fully functional parts in a wide range of materials including ceramic, metallic, polymers and their combinations in form of hybrid, composites or functionally graded materials [3]. The following map (Figure 1) shows the most common materials for biomedical applications and their use in 3D printing technique.

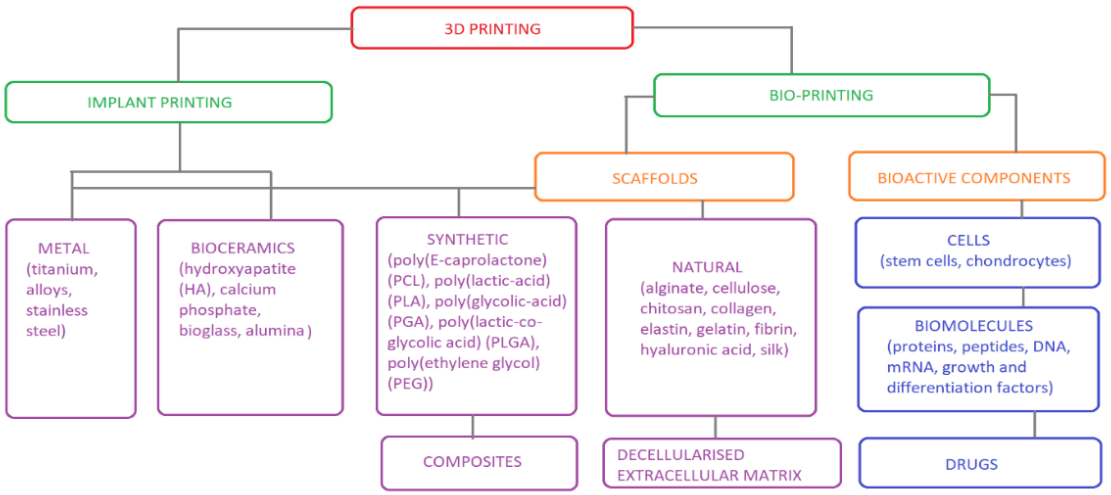

Figure 1: Materials and their biomedical applications [4].

AM processes that are currently used for medical applications can be grouped into two categories according to the raw material: polymers and metals. Selective laser sintering (SLS), stereolithography (SL), and fused deposition modeling (FDM) are the most common AM techniques for polymers, while SLM and electron beam melting (EMB) are those for metals. Table 2 shows the most common AM techniques and respective materials, their feedstock, heat source and applications.

AM Method	Material	Feedstock	Heat Source	Application
Stereo lithography (SLA or SL)	Photo polymers	Resin	UV laser	Molds, patterns, prototypes
Fused deposition modeling (FDM)	Thermoplastic polymer	Filament	Heating chamber	Antibiotic delivery systems, porous structures, scaffolds
Selective laser sintering (SLS)	Metal, polymer, ceramic materials	Powder	Laser	Craniofacial and joint implants, scaffolds for tissue engineering
Selective laser melting (SLM)	Metal materials	Powder	Fiber laser source	Cervical, vertebral body replacement, porous dental implants
Electron beam melting (EBM)	Metal materials	Powder	Electron beam	Knee and hip implants, press fit

Table 2: AM technique and relative characteristics.

Depending on the type of the 3D printing technology, the printability of the material is crucial as it leads to precise deposition with chosen spatial and temporal control. This material property is affected by certain processing parameters, the most prominent one being the nozzle gauge and diameter, which regulates the shear stress to which cells are subjected and the time needed for the arrangement of the desired 3D structure, the nozzle temperature, envelope temperature, layer height, extrusion width, air gap, build direction, part or rater orientation, raster angle, filling pattern, and filling percentage. All these parameters could affect the strength by affecting thermal history and size of voids [5].

The significant number of researches in recent years underscores the importance of AM in enabling the future of healthcare. In particular, the AM technology has already established a new approach in the manufacturing and design of customized medical devices that is positively affecting the efficacy of the clinical products. In addition, the processing of functional and specialized biomaterials through AM allows better functional integration, design flexibility, and clinical product optimization. However, there are challenges and issues in-terms of inadequate mechanical properties in 3D printing, scaling up of the AM products for mass production, developing smart printable biomaterials, and vascularization in 3D bioprinting demand innovations. It is reasonable to assume that in the future the healthcare sector can expect new paradigms in AM technologies [6].

1.2) Fluid Deposition Model (FDM)

Fused Deposition model (FDM) is known as Solid-based AM technology which is mainly used for modeling, prototyping and production applications. It was developed and commercialized by Scott Crump and Stratasys, which works under the controlling of Stereolithography (STL) file. In this process, FDM printers use a continuous filament of a thermoplastic material in a material extrusion method that is heated to the melting point temperature; molten material from the printhead nozzle is deposited on the surface of the growing workpiece to create 3D structures. The nozzle and substrate are controlled by computer to print defined shape and structure, and nozzle can be travelled in both horizontal and vertical directions. Using computer-aided

technology, FDM is very flexible to print 3D objects [7]. Figure 2 shows on the left a 2D schematic representation of printer and its components and on the right the simplified process flowchart of the FDM process.

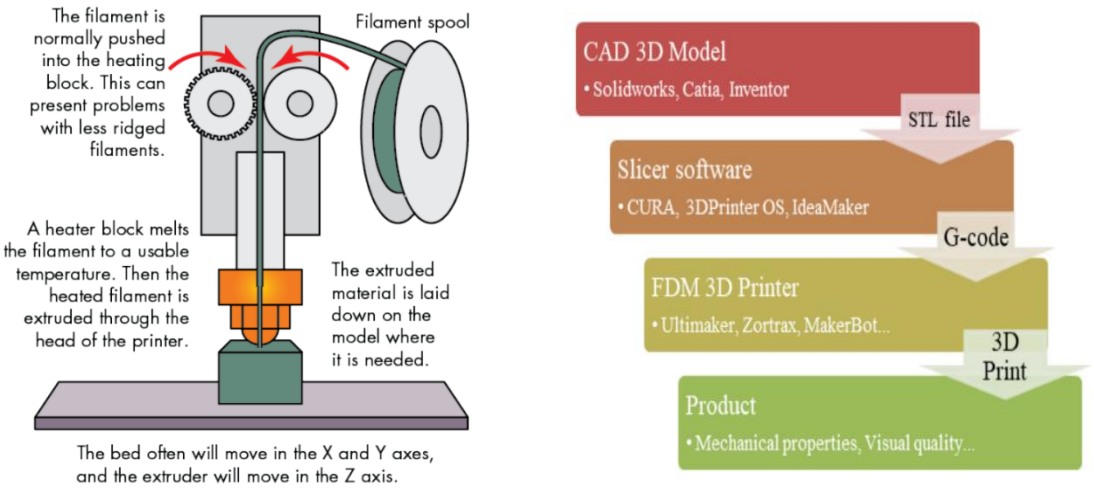

Figure 2: Schematic 2D representation of FDM printer and its flowchart process [8].

The process starts with the creation of the sample design through specific CAD program, then the project is exported as .stl file and imported in a software linked to the printer. This type of software allows to set parameters useful for a desirable sample production and to transform the .stl file in a .gcode file, importable directly inside the printer thanks to an external memory.
FDM used the thermoplastics Polylactic Acid (PLA), nylon, polycarbonate (PC), and polyvinyl alcohol (PVA), that are some of the other commonly used printing filaments. Table 3 shows a panoramic of the most used material in FDM technique with their pros and cons.

MATERIAL	PROS	CONS
Polylactic Acid (PLA)	Biodegradable and made from sustainable sources, inexpensive, does not produce fumes while printing, does not warp.	Poor mechanical characteristics, naturally disintegrates over time.
Acetonitrile Butadiene Styrene (ABS)	Superior toughness, impact resistance, and chemical stability, good thermal stability, can be finished via an acetone vapor bath (that is one of the easiest ways to get a smooth finish out of a completed 3D printing project), inexpensive.	Highly prone to warping, gives off toxic fumes.
Polyethylene Terephthalate (PET)	Chemically stable, good flexibility and impact resistance, good optical properties.	Tough to finish, expensive.
Nylon	Very strong, yet flexible, heat-stable.	Prints at very high temperature, prone to warping, degrades under UV radiation.
Thermoplastic Polyurethane (TPU)	Rubber-like flexibility, excellent layer-to-layer adhesion.	Difficult to handle, poor bridging performance, cannot be smoothed or polished.
Polycarbonate (PC)	Strong, flexible, and heat-stable, good optical properties.	Requires very high printing temperatures, prone to abrasion.
Polyvinyl Acetate (PVA)	Dissolves in water, good bed adhesion, breaks down into non-toxic compounds.	Compatible only with low-temperature filament, quickly breaks down over time, requires a dual extruder printer.
High-Impact Polystyrene (HIPS)	Prints at high temperature, dissolves in limonene, can be used a standalone filament.	Prone to warping, emits styrene while printing, requires a dual extruder printer.
Polypropylene (PP)	Excellent strength and impact resistance, heat-resistant and chemically stable.	Prone to warping, extremely poor bed adhesion.
Polyethyl Ether Ketone (PEEK) and Polyether Imide (PEI)	Good rigidity and strength, thermally and chemically stable.	Requires very high printing temperatures, requires extraordinary measures against warping, limited availability, expensive.
Amphora	Strong and flexible, good bridging performance, safe for food contact, less tendency to warp.	Expensive, high printing temperature.
Composite filaments	Superior aesthetics, wide finishing options.	Brittle filament accelerates wear on the nozzle, poor bridging performance.

Table 3: Pros and cons of some polymeric materials used for 3D printing.

In general, the advantages of this technique include its low cost, the lack of use of organic solvent, the ability to form a fully interconnected pore network in complex 3D architecture, and rare or no requirement of cleaning up the finished objects. This technique allows a flexible fabrication of interconnected porous scaffolds with compositional or morphological variation across the entire matrix, with architecture being highly reproducible. Nonetheless, there are inherent limitations of raw material selection, which needs to be used in the form of filaments with specific size. Other limitations include the effect of high temperatures on raw material, and the lack of adequate resolution [9]. Ideed, the materials used for 3D printing must take into account variety, composition, strength, and finishing procedures in order to increase the versatility of the technology. Currently, the variety of materials is limited to the ability of the materials to be powder-based or have low enough viscosities to be extruded from the printing head. Many manufacturers require proprietary materials to be used in their 3D printers or risk forfeiting the warranty. This scenario has limited the material pool, and thus, for 3D printing to continue to grow, the quantity and diversity of materials must increase [10].

The future of this technology looks to the ability to use 3D printing to enhance business operations, reduce costs and improve efficiency, and it is exactly why 3D printing has become a popular solution. As it continues to grow, FDM 3D printing will continue to become a leading technology that is embraced by businesses around the world because printers can really enhance the simplicity of the whole worker process.

1.3) Mechanical property of material

In this chapter is useful to introduce the measures typically used for engineering materials, in particular the ones used for assessing material mechanical behavior in response to loading. Thus, the primary interesting biomechanical properties describe the relationship between loads (forces) applied to a specific material test specimen and the deformations that result from the applied loads. Also, to study the material behavior without regard the effect of geometry, other two important biomechanical measurements are introduced: stress (σ) and strain (ε). They are

obtained converting the load values to stress values and converting the deflection values to strain values through the equations (1) and (2):

$$\sigma = \frac{Force}{Original\ Area*(1-Porosity)} \qquad (1)$$

$$\varepsilon = \frac{Deformed\ lenght - Initial\ lenght}{Initial\ lenght} * 100 \qquad (2)$$

The stress describes the intensity of the application force experienced by the sample while the local deformation that results from these applied loads is referred to as strain. Unlike displacement, the deformation is expressed in terms of a relative change in the size or shape of the specimen.

Key mechanical variables can be identified on the load–deformation or stress–strain curve, presented in Figure 3. The load–deformation curve describes the amount of load needed to produce a unit of deformation and reflects the structural behavior of the material. Load and deformation are linearly related until the yield point is reached, at which point the slope of the load–deformation curve decreases. Before the yield point, the material is in the elastic region, and if the applied load is removed, the material will return to its original shape with no permanent or residual deformation. The slope of the load–deformation curve in this elastic region defines the structural stiffness of the material. In contrast to the elastic region, in the post-yield region, the material undergoes permanent deformation and does not return to its original shape if and when the load is completely removed. If the load continues to increase, the ultimate or failure load is reached after which point the structure fails or fractures. The energy required to cause failure of the structure is calculated as the area under the stress-strain curve under gradually increasing load. The ability of a material to absorb energy and plastically deform without fracturing is called toughness. It is a property that is indicative of a material's resistance to fracture when a crack (or another stress-concentrating defect) is present.

The stress–strain curve is similar to the load–deformation curve but reflects the material behavior.

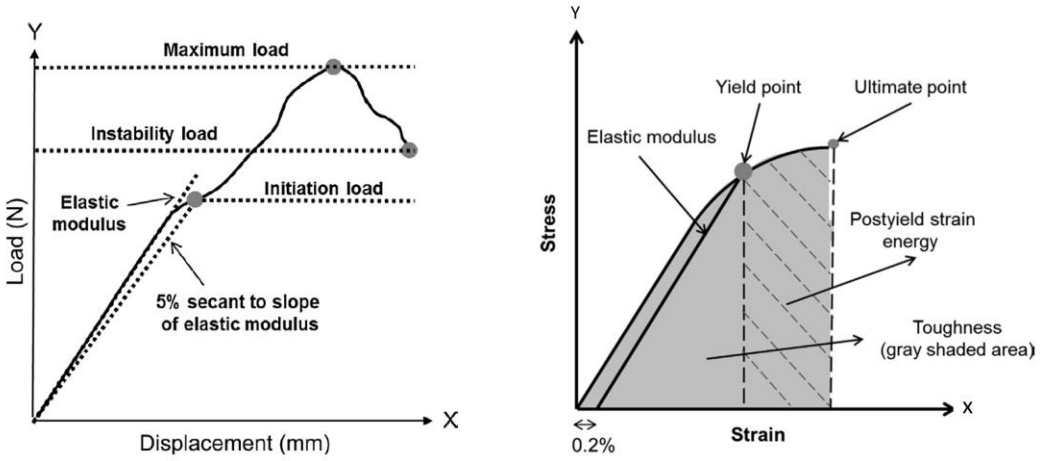

(a) (b)

Figure 3: General mechanical values in (a) Load-Displacement and (b) Stress-Strain curves [11].

A stress–strain curve is generated by conducting a mechanical test on a specimen of standardized geometry, such that one can easily determine stress from force and strain from displacement. Initial loading exhibits linear behavior, and the slope of the stress–strain curve in this elastic region is the elastic (or Young's) modulus $E = \frac{\sigma}{\varepsilon}$ (3).

The amount of strain will undergo in response to an applied stress depends on the Young's modulus. It is the slope of the initial portion of the stress–strain curve. The values of stress and strain at the yield point are the yield stress and yield strain, respectively. Although there are several methods acceptable for determining the yield point, one commonly used method is to define the yield point as the location at which a line having the same slope of the elastic modulus intersects the stress–strain curve and has a strain intercept of 0.2%, as shown in Figure 3b. This point demarcates the separation between linear-elastic behavior and irrecoverable plastic strain. Variables that are computed prior to the yield point are considered pre-yield while those beyond the yield-point are considered post-yield. The point of maximum stress on the curve is the position at which the material begins to reach failure because the material cannot sustain any additional load beyond this point. The values of stress and strain at this ultimate point are the ultimate stress and ultimate strain.

1.4) Lattice structures

Lattice structures are crystal structures where nodes are connected in the form of a lattice to form a specific configuration. In the context of additive manufacturing lattice structures play a more and more important role due to their strong design. The design is defined by the unit cell, which often falls into one of two categories: strut and surface based (Figure 4).

Strut-based unit cells consist of a network of often prismatic struts connected at nodes, similar to truss structures. Surface-based unit cells are mathematically defined as the surface connecting set of points for which a given function has a constant value, that is an isosurface.

Unit cell design holds large influence over the mechanical properties of a lattice structure. In strut-based unit cells, the connectivity of the struts, that is the number of struts connected at a given node, greatly controls the structure's behavior under compressive load. For low or high connectivity, unit cells exhibit what is known as bending- or stretch-dominated behavior, respectively. Bending-dominated structures are desired for applications where mechanical energy absorption is required. Stretch-dominated unit cells are preferred for structural applications, due to greater stiffness and yield strength. Common examples of strut-based lattices are the body- (BCC) and face-centered cubic (FCC) structures (Figure 4a, 4b) which are bending and stretch dominated, respectively.

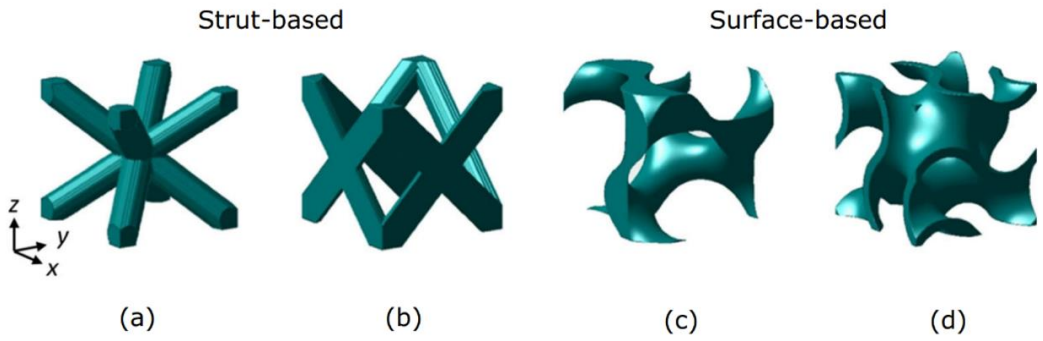

Figure 4: Types of unit cells, in particular (a) body-centred cubic, (b) face-centred cubic, (c) gyroid (skeletal/network) and (d) double gyroid (sheet/matrix) [12].

The most common types of surface-based unit cells are the triply periodic minimal surfaces (TPMS), where "triply periodic" means that the structure can be packed together in a periodic 3D pattern and "minimal surface" means that it locally minimizes surface area for a given boundary such that the mean surface curvature at each point is zero (a closed curve lying on the surface). With planar curves, these surfaces are planar. With three-dimensional curves, these surfaces do not present discontinuities, thus resulting in extremely smooth surfaces.

TPMS has been mathematically created using level-set equations derived from the level-set method (LSM), a methodological framework primarily used for numerical analysis of surfaces and shapes. Those equations consist of implicit trigonometric functions that define an isosurface. Classical examples of TPMSs include Schwartz surface, Gyroid surface and Diamond surface which can be characterized through implicit functions reported above with their respectively representations (Figure 5) as follow:

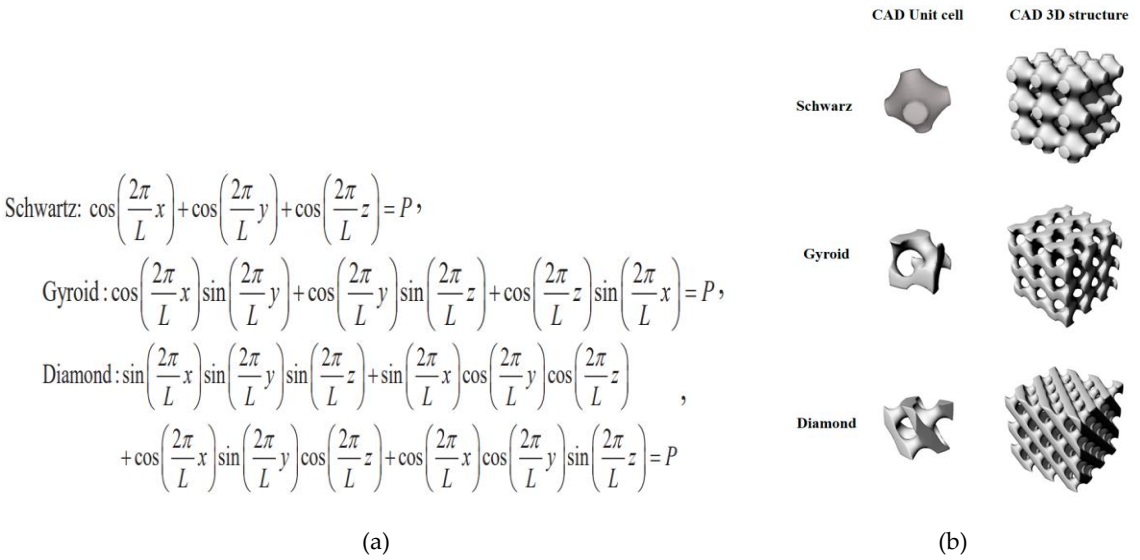

Figure 5: (a) TPMs' functions and (b) their CAD unit cell and CAD structure [13].

P is a constant determining the relative density of porous materials, L is the length of the minimum duplicated cubic unit cell, and x, y, and z are the coordinates of three orthogonal directions, respectively [14]. TPMS unit cells can be further distinguished between those with isosurfaces that have been thickened (sheet/matrix-TPMS), or their enclosed volume solidified (skeletal/network-TPMS), as shown in Fig. 4c, 4d. Some TPMS designs appear to possess good

mechanical features, as is the case for the skeletal/sheet gyroid (Figure 4c and 4d), currently studied for applications such as biomedical implants. Additionally, there are custom designs outside of strut-based and surface-based forms, for example those produced using topology optimization and with internal resonators for vibration isolation.

1.5) Gyroid structure

As mentioned before, one of the most used architectural shape for the biomedical applications is the gyroid triply periodic minimal surface, sheet or skeletal, discovered by Schoen in 1970.
Indeed, researchers have experimentally shown that the gyroid architecture is suitable for biomorphic scaffold design in tissue engineering thanks to its mechanical properties. Particularly, Kapfer et al. [15] demonstrated that the sheet based gyroid structure has higher stiffness than the network-based gyroid structure at the same porosity of the same material. Similarly, AlKetan et al. [16] investigated the mechanical properties of a wide range of structures, including strut-based, skeletal-TPMS and sheet TPMS porous structures, and concluded that sheet-TPMS structures have superior mechanical properties in terms of stress and strain responses (Young's modulus). Sheet-based gyroid structure also has relatively higher Young's modulus, peak stress, and toughness in comparison with skeletal gyroid structure and it shows good mechanical performance [17]. Other comparison from literature between skeletal and sheet-based gyroids scaffold, with the same unit cell sizes, show that the sheet thickness is much lower than the skeletal gyroid "strut thickness" [18].
In the gyroidal scaffold every unit cell is characterized by its relative density ($\bar{\rho}$), which is defined as the ratio of the density of the unit cell material (ρ) calculated as the mass of the structure (m) divided by its volume (V), to the density of the base (solid) material (ρ_0): $\bar{\rho} = \frac{\rho}{\rho_0}$ (4)
Therefore, the relative density of the unit cell, often called volume fraction, is a design feature of key importance, largely controlling the mechanical properties of the structure. The relative density essentially defines how much solid material is present in the overall volume occupied by the cellular material.

The complement to unity of the relative density is porosity (P), that is the percentage of void space in a solid structure, and it can be calculated by the gravimetric method, given by equation (5):

$$P = 1 - \bar{p} = \left(1 - \frac{p}{p_0}\right) x100. \quad (5)$$

Another key property of the lattice structure is the pore size, evaluated as the diameter of sphere that can be inscribed inside each cavity (void) of the TPMS unit cell, as shown in Figure 6:

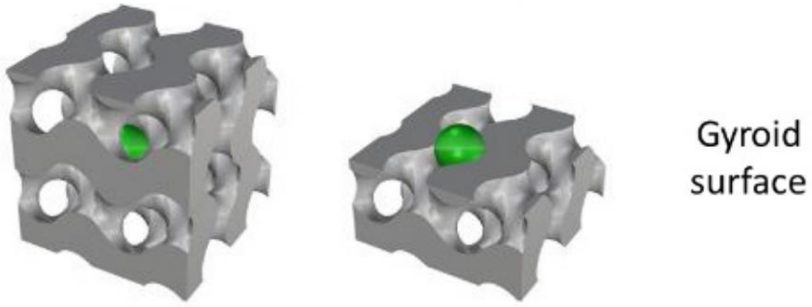

Figure 6: Gyroid surface and its pore size [19].

Generally, for replicate bone scaffolds, the pores size should be maintained in a given range (150 ÷ 600 μm). Porous materials with a specific pore size facilitate growth of cells. For example, pore sizes of ~5–15 μm were considered suitable for fibroblast,76 ~70–120 μm for chondrocytes,77 ~100–400 μm for osteoblast ingrowth [20].

In some cases, an increase in pore size can also reduce the Young's modulus and yield strength, due to wall thickness thinning. This compromises the structural integrity of the scaffold. Balancing the biocompatibility with the mechanical properties is a prerequisite in the development of a superior biomaterial device.

Although the pore size is an important parameter for the control of the biological response to porous in-growth structures, it can be considered as a function of the unit cell size. For example, in order to produce high porosity material of relatively small unit cell size the strut thickness of the constructs must be minimized.

Therefore, the interest of this work is to analyze three factors which determine the properties of the gyroid lattice structure: wall thickness, unit cell size and the porosity. The fact that these factors can all be independently modified allows to create different structures with the same base cell geometry but with selectable and controllable physical and mechanical properties.

1.6) Bone

Bone has a varied arrangement of material structures at many length scales which work in concert to perform diverse mechanical, biological and chemical functions such as structural support, protection and storage of healing cells, and mineral ion homeostasis. Scale is of importance in discussing bone architecture as the structure is hierarchical and complex. In order to understand the mechanical properties of bone material, it is important to understand the mechanical properties of its component phases, and the structural relationship between them at the various levels of hierarchical structural organization [21]. These levels and structures are:

(1) the macrostructure: cancellous and cortical bone;

(2) the microstructure (from 10 to 10 mm): Haversian systems, osteons, single trabeculae, lamellae;

(3) the nanostructure (from a few hundred nanometers to 1 mm): fibrillar collagen and embedded mineral;

(4) the sub-nanostructure (below a few hundred nanometers): molecular structure of constituent elements, such as mineral, collagen, and non-collagenous organic proteins.

This hierarchically organized structure has an irregular, yet optimized, arrangement and orientation of the components, making the material of bone heterogeneous and anisotropic (Figure 7).

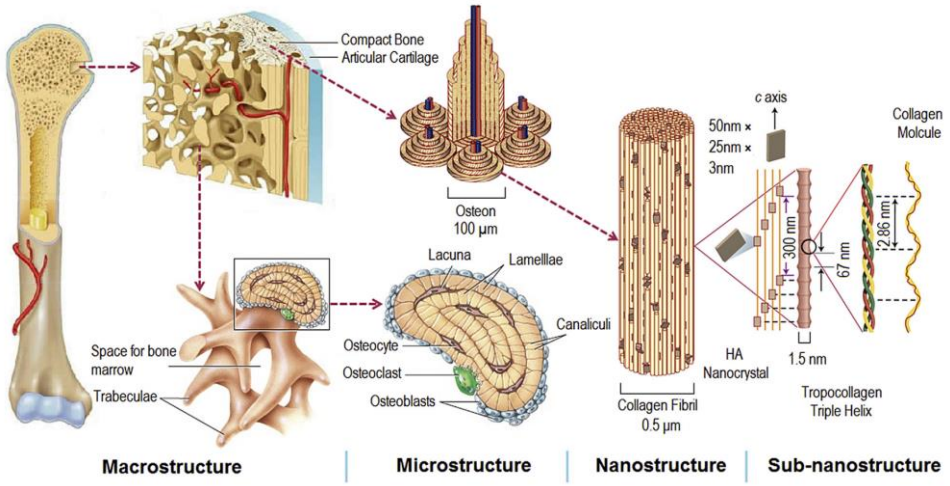

Figure 7: Hierarchical organization of bone [22].

From a material science point of view bone matrix is a composite material of a polymer-ceramic lamellar fiber-matrix and each of these design and material aspects influence the mechanical properties of the bone tissue. The mechanical properties depend on the bone composition (porosity, mineralization etc.) as well as the structural organization (trabecular or cortical bone architecture, collagen fiber orientation, fatigue damage etc.). General mechanical properties of the two types of bone tissue, namely the cortical bone and cancellous bone are shown in Table 4.

Type of bone	Compressive strength (MPa)	Flexural, tensile strength (MPa)	Strain to failure (%)	Young's Modulus (GPa)
Cortical bone	100-230	50-150	1-3	7-30
Cancellous bone	2-12	10-20	5-7	0.8-0.05 (vertebra 0.0067±0.045, tibia 0.445±0.257, femur 0.441±0.271)

Table 4: Mechanical properties of human bones, average values from literature [23, 24].

In Biomedical Engineering's field, bone can be replaced through Scaffolds. Scaffolds serve as three-dimensional structures to guide cell migration, proliferation and differentiation. In load bearing tissues, it also serves as temporary mechanical support structure and it should respect specific requests. Indeed, an ideal scaffold should be mechanical capable, bioresorbable, biocompatible and supportive to cell attachment, proliferation and differentiation. Biocompatibility is the first concern for scaffold fabrication, because scaffolds are external substance which might cause rejection and harm to the human body. Also, biomaterials used to fabricate scaffolds must be safe: no induced inflammatory response, extreme immunogenicity, or cytotoxicity to native cells, tissues, or organs. Another important characteristic is that the scaffold must be degraded to allow cell to produce their own extracellular matrix (ECM), therefore it is not intended as permanent implants. Biodegradation rate of fabricated scaffolds should be similar to the pace of tissue formation in human body, so scaffolds should generate constructs mimicking tissues or organs to be replaced and ideal mechanical integrity to function from the beginning period of implantation to the completion of remodeling process. For these reasons, scaffold needs to replicate as closely as possible in the composition, structure, and function which could transfer

the loading function to fully replace newly formed tissue after degradation [25]. Therefore, for modelling such scaffolds, specific lattice structure designs are needed and studied in the following chapters to conceive extremely complex requests.

1.7) Digital Image Correlation (DIC)

Digital image correlation (DIC), in particular the two dimensional (2D) DIC, is an innovative non-contact displacement measurement technique which provides great potential for measuring the surface deformations and strains by comparing the digital images of a specimen surface taken during undergraduate laboratory experiments. This innovative particle tracking method has several advantages including simple experimental setup and specimen preparation, ability to work in ambient light with no special illumination, and great measurement accuracy. The main limitations of the DIC method, however, is that the specimen surface has to be planar with a random pattern on the surface. The implementation of the DIC method requires three consecutive steps:

1) specimen preparation and experimental setup;

2) recording images of the planar object during the experiment;

3) processing of the images using a correlation algorithm through a computer program.

Figure 8 shows schematically the DIC measurement setup for in-plane displacement measurements [26]. The camera needs to be mounted perpendicular to the object surface with its optical axis on the geometric center of the specimen. The specimen surface must be planar and most importantly remain in the same plane perpendicular to the camera axis during the experiment. The specimen surface must have a random pattern (texture) to provide a random gray value intensity distribution on the recorded images. The pattern can be either from the natural texture of the specimen surface or from an artificially made pattern such as a painted surface. The pattern deforms together with the specimen surface and carries the specimen's deformation. The 2D-DIC system is only capable of measuring in-plane deformations and any out-of-plane deformations on the specimen surface are neglected. The measurement accuracy

depends on the quality of the images taken during the experiment and there should be no geometric distortion on the images.

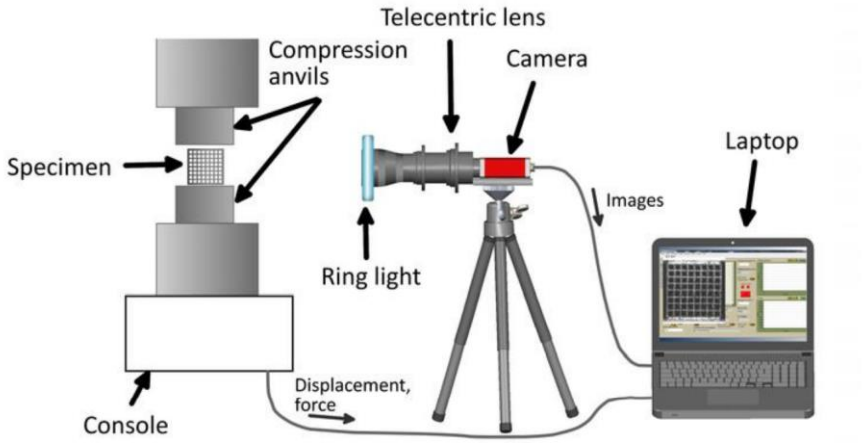

Figure 8 : Typical DIC setup for in-plane displacement measurement [27].

After recording the digital images of the specimen surface during the experiments, DIC compares the acquired images and computes the motion of small regions of each image using a correlation algorithm. The technique relies on a direct correspondence between the displacements in the images recorded by the camera and the deformations of the specimen surface. The image taken before deformation at the beginning of the test is called the reference image and is used as the basis for comparison with images taken during deformation or loading.

1.8) Finite Element Analysis (FEA)

Finite Element analysis (FEA) is a computer-aided numerical analysis program that simulates the behavior, assessed using the finite element method (FEM), of a part or assembly under given conditions. FEA is used to solves complex problems in many engineering fields, like thermal analysis, structural analysis such as stress distribution, vibration, and deflection in complex geometries, and fluid dynamic analysis such as turbulent and laminar flow. Using FEA, a physical phenomenon close to real behavior is simulated and solutions to problems that are anyway difficult to solve are found. To calculate certain behaviors with FEA it is necessary to divide the

geometry into smaller regular shapes (elements), usually noded triangles or quadrats, creating a mesh of millions of smaller elements. Each of these small elements is subjected to calculations and they are finite in nature because their size is highly relevant for the outcome of FEA: smaller elements generate more precise calculations for the overall structure that is to be analyzed.
In general, finite element analysis is a part of the manufacturing process in order to predict how an object would react to real-world conditions when used and also it helps to predict and improve the quality and function of an object.

1.9) Project & Procedure

The thesis project will consist of evaluating mechanical properties of gyroid structures by analyzing their different characteristic with FEA, DIC and testing 3D-printed prototypes in a compression test. The results are then compared and verified with regards to the relation between structural characteristics like porosity, dimension of unit cell size and wall thickness. This because most research about lattice structures focus on their topology optimization or in one or two of the three structural characteristics just mentioned. The aim of this work is to compare and study the three structural characteristics all together. To achieve this goal, the project is organized into six different stages as shown in figure 9.

Figure 9: Flowchart for completion of project in six steps.

The project starts off with a literature study to acquire the necessary knowledge and theory. Previous modules contribute to understanding the project's theory, but a few topics must be studied first before being able to start working on the actual problem of the project. Examples that are studied are TPMS, gyroid structures and how these are modelled using 3D-CAD. To ensure a minimal deviation in the 3D-printed parts, a study on how process parameters affect printed components' properties is made. This is followed up by determining what range of

porosity, wall thickness and dimension of unit cell size are to be used in the experiments. Initial modelling and printing tests are carried out to ensure that all models are manufacturable. After clear constrains have been set for the project, the models have been produced and tested in a compression machine. Further analyzes such as DIC and FEA are also conducted. The results from physical tests and computational analysis have then been studied and used to describes the relationship between the structural characteristics of samples.

Chapter 2: Material & Methods

This chapter focuses on the characteristics of Poly-Lactic Acid, the material used for the production of the gyroid lattice structures, and on the specific process parameters of these samples. Also, the methodologies used to produce the specimens, their physical testing, and the explanation and the set up for the finite element analysis and the digital image correlation, respectively, are presented.

2.1) Poly-Lactic Acid (PLA)

Polylactic acid or polyactide (PLA) is a biodegradable and bioactive polyester made up of lactic acid building blocks. It was first discovered in 1932 by Wallace Carothers by heating lactic acid under vacuum while removing condensed water. During the early times, only low-density PLA was produced. By using lactide as a raw material and through the process of ring-opening polymerization, a high-density version of PLA was finally developed.
PLA is a polyester (polymer containing the ester group) made with two possible monomers or building blocks: lactic acid, and lactide. Its general property is shown in Table 5 while its chemical formulae in Figure 10.

Property	Value
Melting temperature, Tm	145-186 ˚C
Glass transition temperature, Tg	50-64 ˚C
Density	1.210-1.430 $gxcm^{-3}$
Cristallinity	37%
Tensile strength	28-50 MPa
Yield strength	70 MPa
Young's modulus	1.2-3 GPa
Elongation at break	2-6%
Poisson's ratio	0.3-0.4

Table 5: General property of PLA.

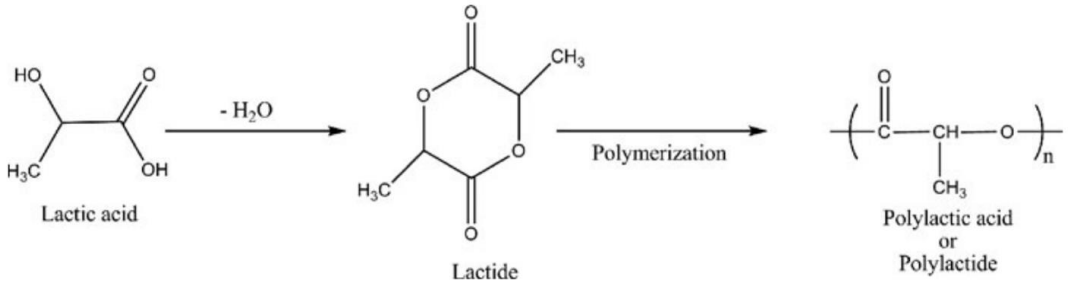

Figure 10: Chemical formulae of PLA.

PLA is widely used in tissue engineering, and it finds a wide spectrum of applications in the medical field due to its ability to be safely absorbed biologically. One of the major advantages of PLA is its biodegradable nature and the sustainable process by which it is made, making it the environmentally friendly choice of plastic. Indeed, PLA and its copolymers are used in the form of implants or devices and can be produced from renewable resources; they are nontoxic to humans as well as to environment. They are being extensively used as biomedical materials in the fields of controlled drug delivery systems, tissue regeneration and as alternatives for other ceramic based polymeric materials which reduce impact on environment. Being a biodegradable material, it avoids surgical procedures to remove the devices of which it is comprised [28].
The most important biomedical applications are reported in Figure 11.

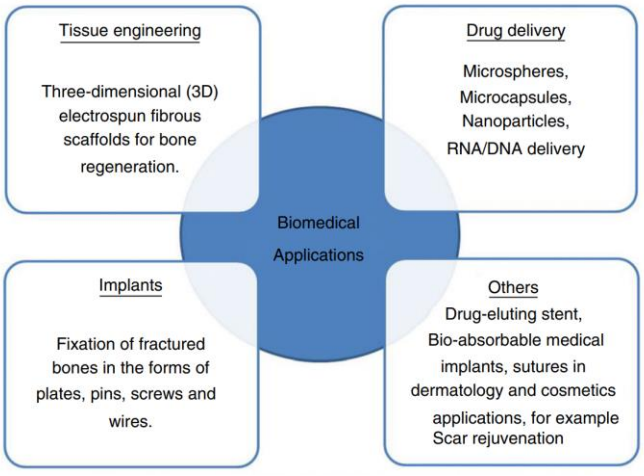

Figure 11: Biomedical applications of PLA [29].

The development of PLA enables its use in various structural and load-bearing application. Fatigue may occur in structural components due to cyclic stress, which leads to catastrophic failure at a lower stress than in the case for the normal static mechanical loading. Understanding fatigue behavior and its damage mechanisms are essential for assessing emerging materials in various applications to determine their durability and long-term reliability. In general, fatigue failure of polymeric materials begins with the initiation of micro defects and crazing in highly stress-concentrated areas. Crazing is caused by internal and external surface defects, voids and poorly bonded matrix interfacial areas, which have a critical effect on the mechanical strength and consequently cause deformation [30].

That work focused on the use of PLA processed in Fused Deposition Modelling because it seems to be an attractive material for reconstructive surgery thanks to its biocompatibility and the possibility to produce individually shaped scaffolds.

2.2) Process parameters of PLA scaffolds

Test specimens are designed and divided into three categories with the dimensional constraints of keeping constant porosity, constant wall thickness, and constant cubic size. Then a total number of 30 cubic sheet-based TPMS gyroid lattices are fabricated from PLA (Polylactic Acid) via FDM technique in order to use them for performed quasi-static compressive test analysis.

The scaffolds are at first designed using SolidWork, which is a software that allows to create and characterize in a 3D way the lattice structure using the parameters mentioned in the paragraph 1.5. The parameters and their respective values are reported in the following Tables (6,7,8):

Number of samples produced	Size structure (mm)	Unit cell size (mm)	Porosity	Wall thickness (mm)
3	16x16x16	4	68.72%	0.645
3	32x32x32	8	68.72%	1.29
3	48x48x48	12	68.72%	1.935
3	64x64x64	16	68.72%	2.58

Table 6: constant porosity of 68.72%.

Number of samples produced	Size structure (mm)	Unit cell size (mm)	Porosity	Wall thickness (mm)
3	16x16x16	4	36.31%	1.29
0	32x32x32	8	68.72%	1.29
3	48x48x48	12	79.23%	1.29
3	64x64x64	16	84.38%	1.29

Table 7: constant wall thickness of 1.29 mm.

Number of samples produced	Size structure (mm)	Unit cell size (mm)	Porosity	Wall thickness (mm)
3	32x32x32	8	84.38%	0.645
0	32x32x32	8	68.72%	1.29
3	32x32x32	8	57.75%	1.935
3	32x32x32	8	36.31%	2.58

Table 8: constant cubic size of 32 mm.

To determinate these parameters, the first step is to find the minimum printable geometry linked to the minimum printable value of the wall thickness. This is obtained through the production of a first cubic sheet-gyroid structure which characteristics are at the beginning taken from literature [31] and then converted to the following values: size of 26 mm, unit cell size of 6.5 mm, wall thickness of 0.838 mm and a porosity of 75%. After its production, other printing tests are made, and it has been established that the smallest printable value for the wall thickness is obtained decreasing by 25% the values just mentioned. Decreasing further the size structure and the unit cell size, and consequently the porosity, the values reported in the first row of the Table 5 have been obtained.

The second step is to find the maximum printable geometry referring to the maximum failure load below 100-kN. This value is the axial capacity of the computer-controlled fatigue testing machine used to perform isothermal fatigue tests with independent bi-axial loading.

From literature [32], a limit value of 51 MPa for the compressive yield strength of PLA samples (structurally similar to those produced in this study) is found and used in the relation (6):

$$\sigma = \frac{Force}{Original\ Area * (1 - Porosity)} \qquad (6)$$

Through this, a maximum printable size structure of 80 mm for cube side is found. It means that the maximum size printable is five times the minimum size printable. For this reason, one sample with size structure of 80x80x80 mm, unit cell size of 20 mm, wall thickness of 3.225 mm and porosity of 68.72% is made and considered as the larger printable one. To understand the validity of these parameters, the strain of the sample within the elastic range is measured. The specimen is directly positioned on the gripper of the testing machine, and it is compressed up to a 3 mm of maximum displacement rate. Other parameters set for the test are 20 Hz as sample rate and 3 mm/min as displacement rate. A second limit of 95 kN is set to protect the instrument from applying a load greater than its capable load. The results show that the maximum value of the axial compression loading is 60.1 kN. So that, the value proposed as the maximum printable geometry is reasonable, but the final size structure of interest for this study is decreased to guarantee a perfect match between the sample and the gripper of the machine. The definitive values considered for the biggest printable sample are 4 times the values of the minimum printable sample and reported in the row number 4 of Table 6.

Row number 2 and 3 in the same table are obtained multiplying the values of the parameters of the smallest sample by 2 and 3 respectively.

The parameters present in Table 7 and Table 8 are acquired keeping respectively wall thickness constant and cubic size constant. In the first case there is an increase in the porosity corresponding to an increase in the size of the geometry, while in the second case there is a decrease in the porosity corresponding to an increase in the value of the wall thickness.

2.3) Specimens fabrication

After the definition of the parameters for the scaffolds, the designed lattices are generated and saved as STL files.

STL files are imported into the slicing software CURA 4.8.0 wherein all the process parameters for the fabrication of the scaffold are adjusted. Among the various 3D printing parameters, the principal ones on which this study focused on to understand the influence on the quality results are reported in the Table 9:

Layer Hight	Infill Density	Speed Retraction	Distance Retraction	Print Speed	Printing Temperature	Build Plate Temperature
0.15 mm	100%	35 mm/s	0.5 mm	50 mm/s	215 °C	75 °C

Table 9: FDM 3D printing parameters.

A layer height of 0.15 mm is selected to achieve a high bond strength between the layers of the printed specimens, while the infill density is chosen as 100% in according to Harshit K. Dave et all. [33] who observed that the compressive strength of the specimen is found to be increasing with increment in the infill density. It may be due to that at higher infill density larger amount of material is consumed to print the part due to a smaller opening in each cell.

After a large number of printing test (Figure 12 (e)), the best values for the speed retraction and distance retraction are respectively 35 mm/s and 0.5 mm. This because retraction is the parameter that allows to combat the stringing, otherwise known as oozing, whiskers, or "hairy" prints. It occurs when small strings of plastic are left behind on a 3D printed model and this is typically due to plastic oozing out of the nozzle while the extruder is moving to a new location. If retraction is enabled, when the extruder is done printing one section of the model, the filament will be pulled backwards into the nozzle to act as a countermeasure against oozing. With the parameters mentioned above, stringing has been quite dammed.

Regarding the print speed, it is the main speed setting that will influence the 3D prints. As the name suggests, print speed determines how fast the motors of the printer move: too slow of a print speed may cause print deformation due to the nozzle sitting on the plastic for too long; too fast can cause overheating artifacts due to insufficient cooling, as well as ringing, under extrusion, and weak layer adhesion. The printing results show that the best value for this parameter is 50 mm/s.

All these parameters have great influence on the porosity and mechanical properties of the printed scaffolds, so also it is necessary to maintain a balance between the temperature and speed of the extruder to print a scaffold with the desired porosity and minimum defects. In this study, the printing temperature and the built plate temperature are set to 215 °C and 75 °C.

Finally, the STL files are sliced and .gcode files that contained the printing instruction are generated, transferred to the 3D printer, and manufactured by this FDM method.

The printer used is called Prusa i3 Mk3. Its characteristics are a diameter nozzle of 0.4 mm, a print heated bed (removable) with a PEI coating and 120 °C as a maximum of print bed temperature, onboard controls, USB and SD card connections, and a maximum extruder temperature of 300 °C. The pros of this printer are the print pause and restart, crash detection, sturdily built and exceptional print quality; the cons are a not exactly reliable long-distance prints and the very dense support structures in the system's default.

The filament used is a 3Dnet black filament with a diameter of 1.75 mm (+/- 0.02 mm), a net weight of 0.75 kg, a gross weight of 1.1 kg, and a printing temperature range of 200 - 230 ° C.

Figure 12 shows in the images and the characteristics of every single printed gyroid lattice structure, the set of samples with constant cubic size, constant wall thickness and constant porosity, and all the trials made before the definition of the final process parameters.

Wall Thickness	0.645 mm
Uni cell size	4 mm
Dimension	16x16x16 mm
Fabrication time	32m

Wall Thickness	1.29 mm
Uni cell size	4 mm
Dimension	16x16x16 mm
Fabrication time	55m

Wall Thickness	0.645 mm
Uni cell size	8 mm
Dimension	32x32x32 mm
Fabrication time	1h37m

Wall Thickness	1.29 mm
Uni cell size	8 mm
Dimension	32x32x32 mm
Fabrication time	3h11m

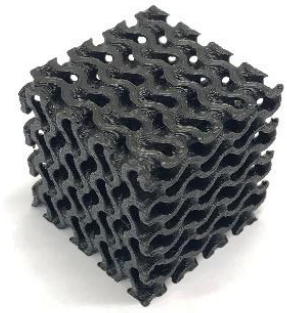

Wall Thickness	1.935 mm
Uni cell size	8 mm
Dimension	32x32x32 mm
Fabrication time	3h54m

Wall Thickness	2.58 mm
Uni cell size	8 mm
Dimension	32x32x32 mm
Fabrication time	5h36m

Wall Thickness	1.29 mm
Uni cell size	12 mm
Dimension	48x48x48 mm
Fabrication time	6h48m

Wall Thickness	1.935 mm
Uni cell size	12 mm
Dimension	48x48x48 mm
Fabrication time	7h2m

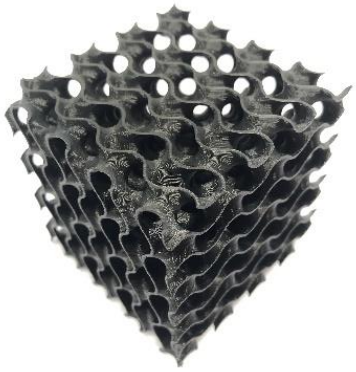

Wall Thickness	1.29 mm
Uni cell size	16 mm
Dimension	64x64x64 mm
Fabrication time	12h52m

Wall Thickness	2.58 mm
Uni cell size	16 mm
Dimension	64x64x64 mm
Fabrication time	18h1m

(a)

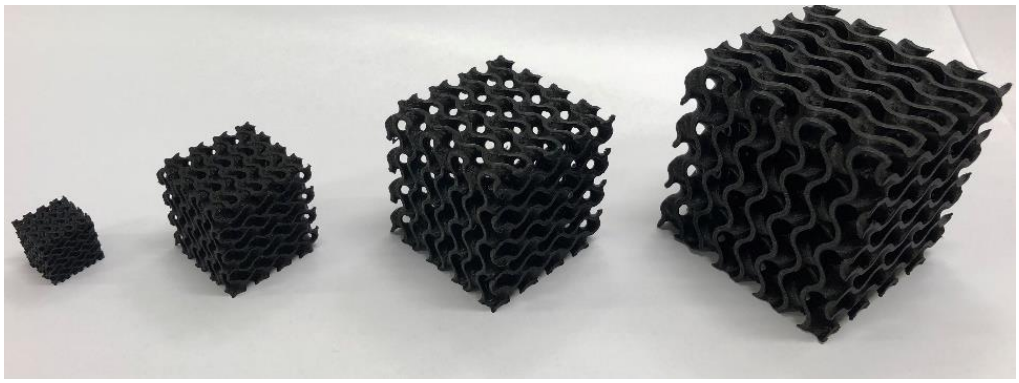

(b)

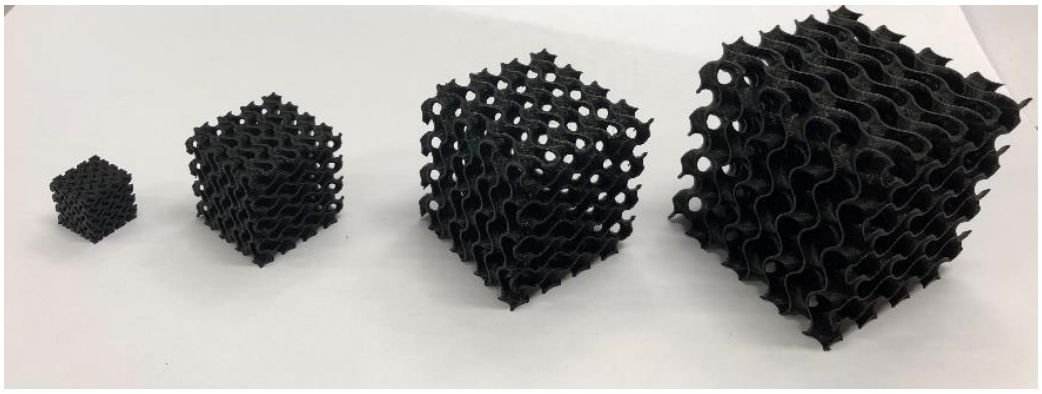

(c)

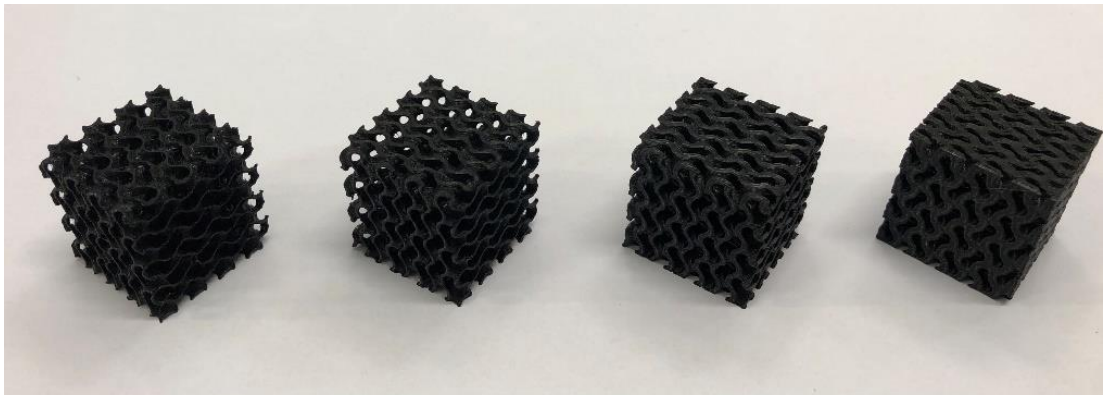

(d)

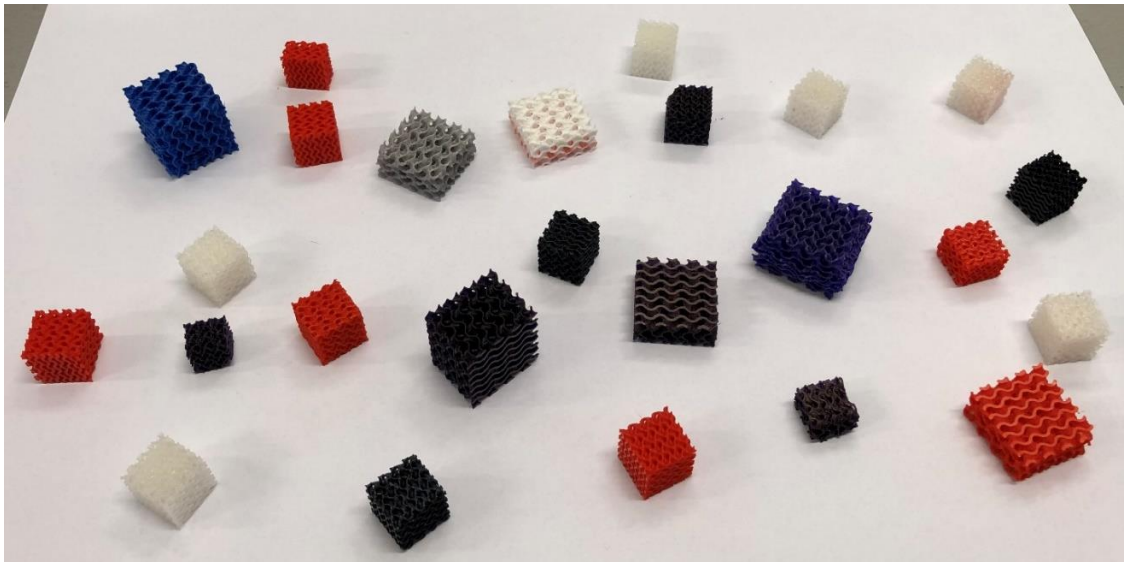

(e)

Figure 12: (a) Images and characteristics of every single printed gyroid lattice structure, (b) set of samples with constant porosity, (c) set of samples with constant wall thickness, (d) set of samples with constant cubic size, constant wall thickness and constant porosity, and (e) all the trials before the definition of the final process parameters.

2.4) Quasi-static compression tests

A servohydraulic MTS 809 machine for mechanical testing is used for compression tests on the fabricated specimens to experimentally investigate failure process and stress-strain response. In the testing device, samples are placed between two plates where the upper plate is fixed while the bottom plate is movable, thereby, they are compressed in parallel to the building direction between the two hardened loading heads. No lubricant is used in the contact surfaces between specimens and plates. The parameters set in the machine are a loading speed of 2 mm/min and a sample rate of 20 Hz. The tests stopped when the load reached 50% of its maximum limit. The compression tests are performed at room temperature and the force measured from the load sensor and the displacement of the moving head are recorded using a computer. Then the data of load and displacement are plotted. To investigate the failure mode of the PLA scaffolds, a camera is applied to record the whole compression processes. For each sample type, three quasi-static compression tests are carried out and the data of these three repetitions are plotted together. From that plots, it is selected which of the three repetition is showing an average value and it is used for the representative plots. For visual clarity, specific names and colors are assigned to every samples and reported in Table 10 with the respective characteristics of the specimens. The writing "letter-number-number" refers to "type of structure (Gyroid)-dimension of unit cell size-value of wall thickness", respectively.

Name of sample	Color on the plot	Geometry Dimension (mm)	Unit Cell Size (mm)	Wall Thickness (mm)	Porosity (%)	Volume Fraction (%)	Yield Strength (MPa)	Young's Modulus (MPa)
G-4-0.645	Light green	16x16x16	4	0.645	68.72	31.28	18.17	892.25
G-4-1.29	Dark green	16x16x16	4	1.29	36.31	63.69	20.15	1051.5
G-8-0.645	Orange	32x32x32	8	0.645	84.38	15.62	14.01	589.2
G-8-1.29	Red	32x32x32	8	1.29	68.72	31.28	23.2	764.2
G-8-1.935	Violet	32x32x32	8	1.935	57.75	42.25	29.1	1008.5
G-8-2.58	Light blue	32x32x32	8	2.58	36.31	63.69	106.82	3898.6
G-12-1.29	Gray	48x48x48	12	1.29	79.23	20.77	17.06	685.27
G-12-1.935	Blue	48x48x48	12	1.935	68.72	31.28	22.45	840
G-16-1.29	Yellow	64x64x64	16	1.29	84.38	15.62	18.27	752.22
G-16-2.58	Pink	64x64x64	16	2.58	68.72	31.28	26.22	770.45

Table 10: Characteristics of every gyroid lattice structures.

2.5) DIC set-up

In this work, in orded to perfor the digital imag correlation analysis, the second set of samples was painted before being subject of the quasi-static compression test. Every samples was painted using a white specific mate paint and an airbrush. The paint has been applied only on a single face of every single spaciment and were left to dry for a couple of hours. Then they were positioned in the compression machine, the DIC is set up and the quasi-static compression test were performed. The software used for the DIC analysis is VIC-2D system, a solution that utilizes optimized correlation algorithms to provide full-field two-dimensional displacement and strain data for mechanical testing on planar specimens. The set up and results for the DIC analysis are showen in the next chapters.

2.6) FEA settings

The gyroid structures are analyzed for their mechanical properties with linear FEM to validate the results of the compression test. FEA is performed using ABAQUS/CAE 2019 (Simulia, Dassault Systèmes). The analysis simulates compression of the gyroids under the same conditions as the compression tests done in the test machine.

Prior to FEA the gyroid cubes are prepared by adjusting the mesh size and removing potential defects in the geometry. The default mesh contains too many elements and mesh size is therefore increased to receive a reasonable number of elements for performing the analysis. Therefore, the .stl files are imported individually in 3D Builder where the number of elements is reduced. Then, the new .stl files are imported in SolidWorks 2020 and converted in .step files. The files are now ready to be analyzed in Abaqus. In particular, the analysis focuses on the linear response of samples which allows to evaluate their stiffness values.

The files are imported as single part in the software and the material property for PLA is assigned with a generic average value of Young's modulus of 2300 MPa and a Poisson ratio of 0.3 (refer to Table 5). To simulate the quasi-static compression test, two boundary conditions are used:

1) a vertical upward displacement applied to the gyroid's bottom surface with a maximum displacement of 0.2 millimeters for samples G-4-0.645 and G-4-1.29, and of 0.5 millimeters for the other samples, to make sure the results match the linear part;

2) an encastre fixed at the top of every object.

The analysis is done individually for every volume fraction with the same settings and material data. The visualization for the representative sample G-8-1.29 is presented above (Figure 13) while the data are reported in the next chapter:

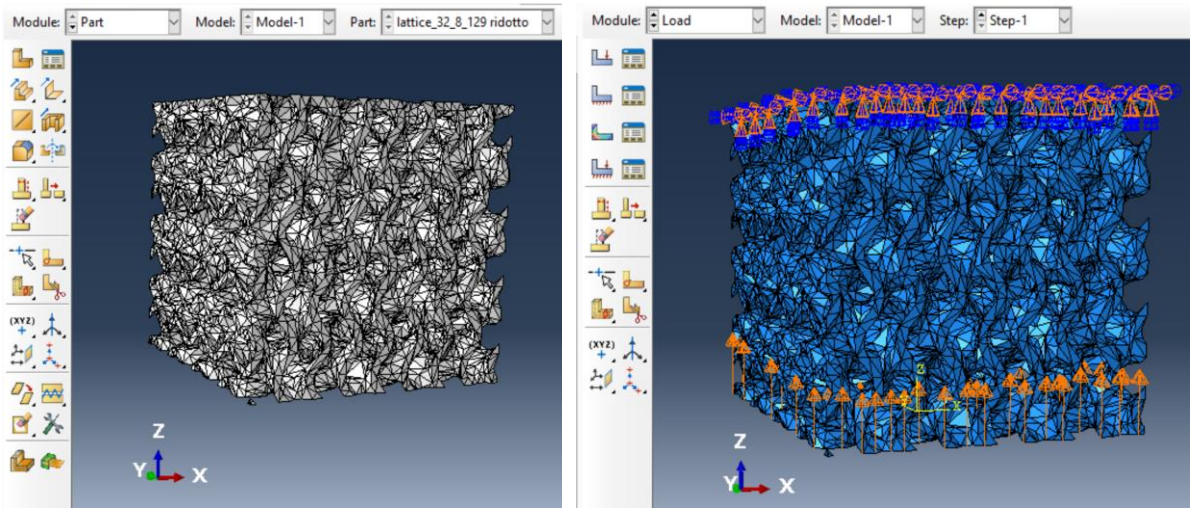

Figure 13: Abaqus visualization of lattice G-8-1.29. On the left: model imported with its mesh. On the right: application of boundary conditions.

Chapter 3: Results & Discussions

Consequently to the experiments, the data of load and displacement are plotted and processed to obtain the data of stress and strain, following what is said in the chapter 1.3. In that way, the stress-strain curves are obtained, and observations are made. Also, the results regarding energy absorption, DIC and FEA are presented and discussed in this chapter.

3.1) Constant cubic size

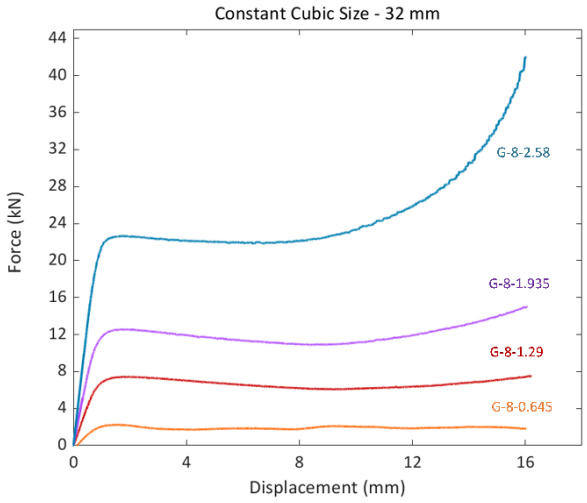

(a)

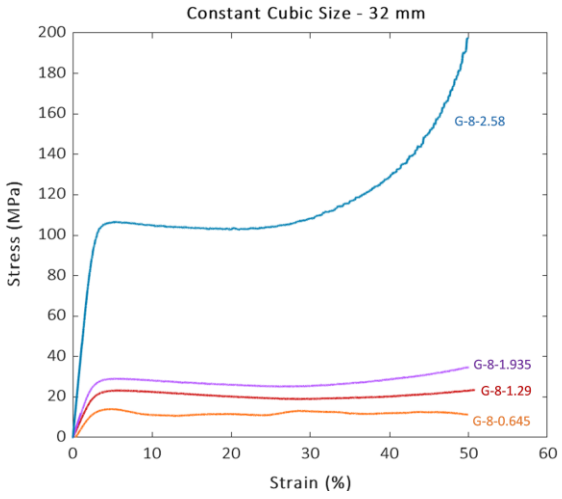

(b)

Sample	Porosity (%)	Yield Strength (MPa)	Young's Modulus (MPa)
G-8-0.645	84.38	14.01	589.2
G-8-1.29	68.72	23.2	764.2
G-8-1.935	57.75	29.1	1008.5
G-8-2.58	36.31	106.82	3898.6

(c)

Figure 14: (a) Load-Displacemente curves, (b) Stress-Strain curves and (c) calculated parameters for set with constant cubic cell size.

The results show that, keeping constant cubic size, the lattice structure with the least volume fraction (higher porosity), has the least compressive strength and the structure with the highest volume fraction (lower porosity) has the highest compressive strength. Indeed, when porosity decrease the compressive strength of the lattice structures increases, and as the volume fraction and the wall thickness increase, the density of the connecting struts in the lattice structure increases. Looking the Stress-Strain curves, they initially climb linearly showing the elastic region. Here the curves can be referred as ductile failure where the unit cells are not catastrophically failed. Then, the trend of the curves begin to concave downward. Such behaviour can be referred as a failure where some unit cells are collapsed or fractured completely. With the increasing load, other connecting cells starts to carry the load which resulted in bearing higher stress of the cellular structure. All the curve, except the one for G-8-0.645, are slowly concaved downward but then they goes up around 30% of strain with an exponential increase in the stress until the end of the test. That phenomenon is called densification and the structure thickens sufficiently for the strands to merge and eventually lead to full densification. The different deformation of sample G-8-0.645 starts to localize beyond the elastic region in consecutive layer-by-layer failures. It leads to several humps in the plateau region where the collapse of each layer is observed as a hump on the stress-strain curve, and the number of humps directly correlates to the number of layers in the direction of compression. This difference in the behaviour can be seen in Figure 15 that shows the progressive deformation of the specimen in specific values of strain:

a) G-8-0.645

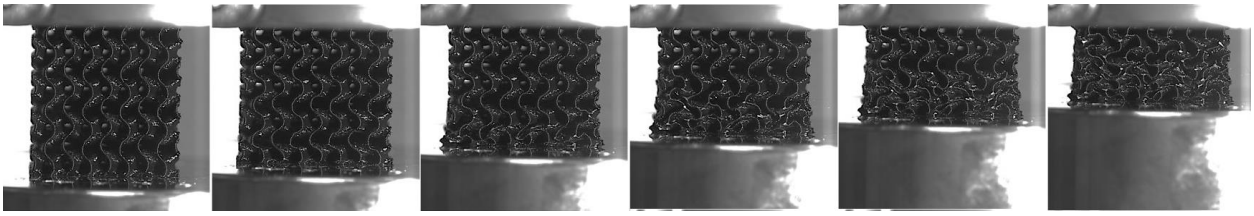

0% 10% 20% 30% 40% 50%

b) G-8-1.29

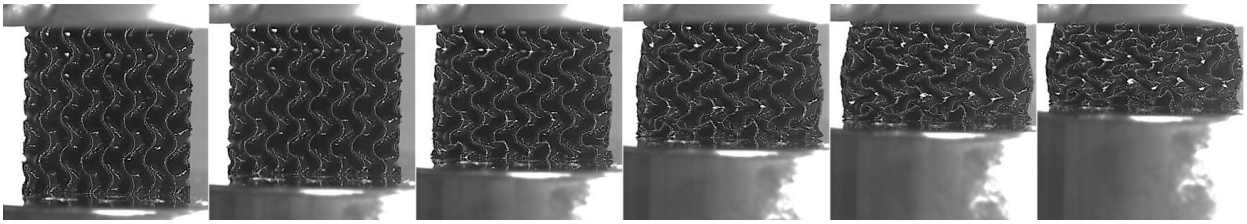

0% 10% 20% 30% 40% 50%

c) G-8-1.935

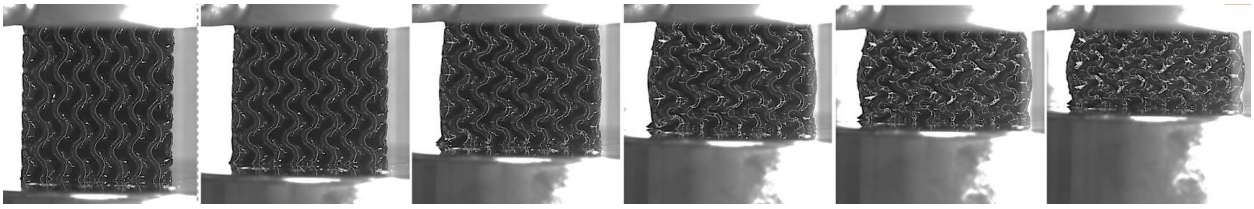

0% 10% 20% 30% 40% 50%

d) G-8-2.58

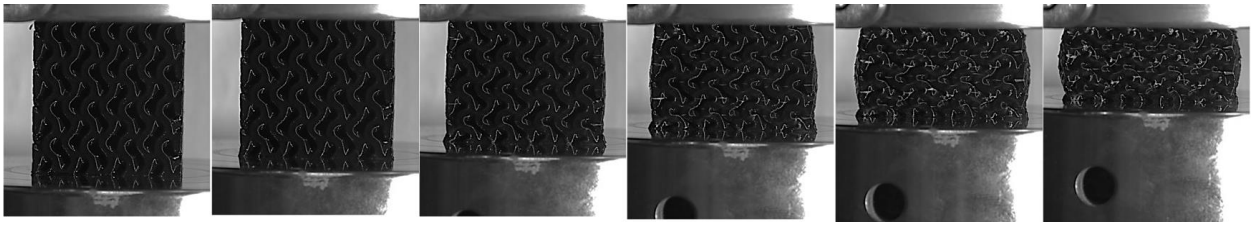

0% 10% 20% 30% 40% 50%

Figure 15: Progressive deformation of the specimen for strain values of 0%,10%,20%,30%,40% and 50%.

After value 20% of strain, the failure of G-8-0.645 consists in successive collapse of cells in planes perpendicular to the manufacturing and loading direction while other samples present a globally uniform deformation mode, featured by probable buckling and folding of the cell-walls under

compressive loading condition and characterized of fracturing of the cell walls by the propagation of cracks through the lattice. This means that for high relative densities, the Gyroid-structure continues to deform more uniformly beyond the elastic region compared to the Gyroid-structures having low relative densities. That was also observed in previous study [34, 35].

3.2) Constant wall thickness

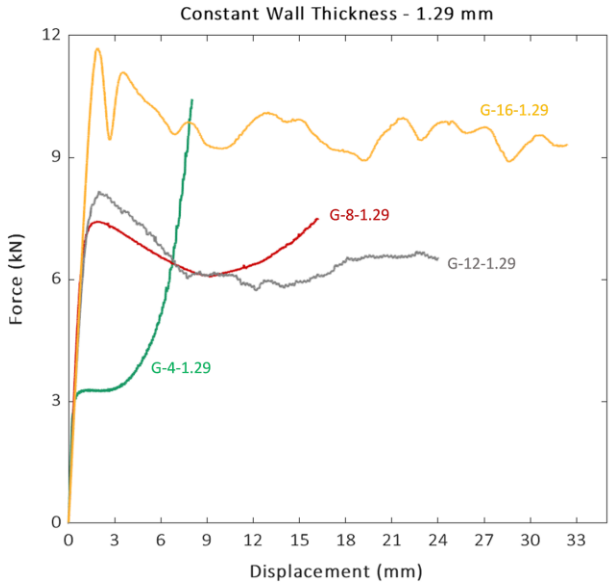

(a)

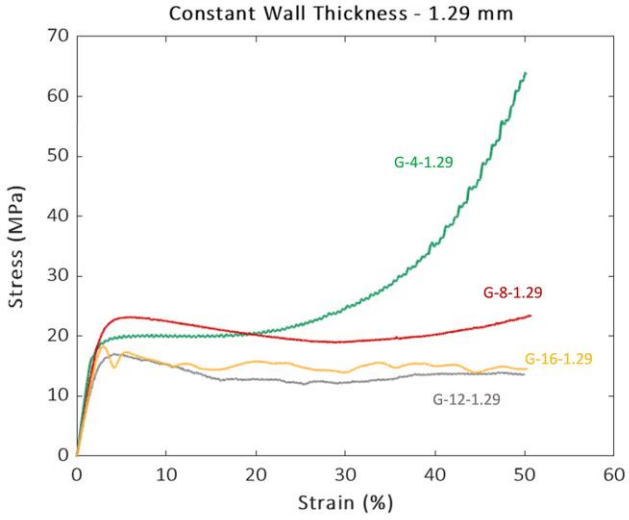

(b)

Sample	Porosity (%)	Yield Strength (MPa)	Young's Modulus (MPa)
G-4-1.29	36.31	20.15	1051.5
G-8-1.29	68.72	23.2	764.2
G-12-1.29	79.23	17.06	685.27
G-16-1.29	84.38	18.27	752.22

(c)

Figure 16: (a) Load-Displacemente curves, (b) Stress-Strain curves and (c) calculated parameters for set with constant wall thickness.

As observed before, usually with increasing porosity, the mechanical strength of scaffolds decreases as it corresponds to reduced material and weakening the system. However, for lattice with 68.72% of porosity, higher value of Yield Strength is obtained than the other three porosity samples, while the highest value of Young's Modulus is obtained for G-4-1.29 with 36.31% of porosity. The reason lies in the fact that porous materials deform either by bending dominated or stretch-dominated mode. Stretch-dominated structures are resistant toward deformations, whereas bending-dominated structures are more energy absorbent. Same results and the same behavior is confirmed from literature [36].

This aims to show that, as mentioned in the capter 2.1, bending deformation is linked to structure with high porosity and low connectivity of the strut, while stretch behavior is tipycal of structure with lower porosity and higher connectivity of the strut. So, for this context, the scaffold with lowest porosity of 36.31% is more like a network of sheets (stretching tendency), whereas the two lattices with 79.23% and 84.30% of porosity act as a network of struts (bending tendency). Intermittently, the 68.72% porous scaffolds have both. A validation can be made using Figure 17 that shows the post-compression shapes of samples with constant wall thickness:

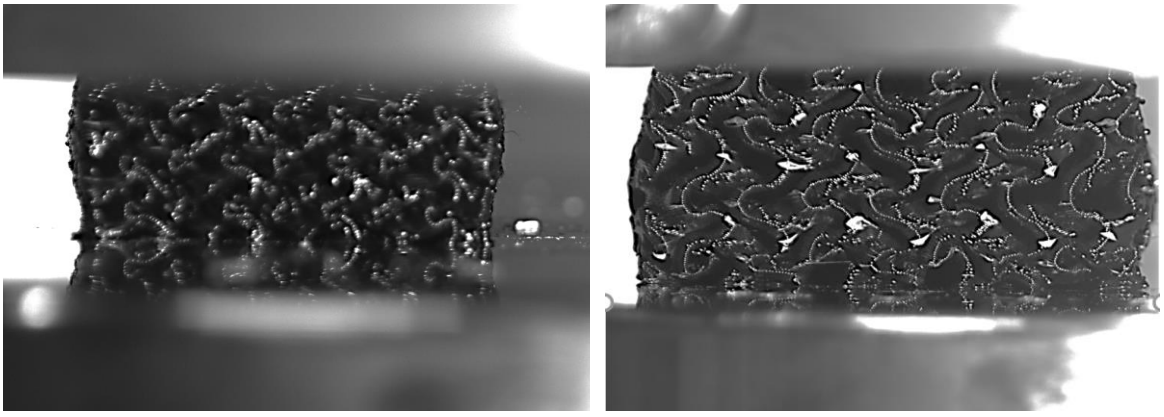

(a) (b)

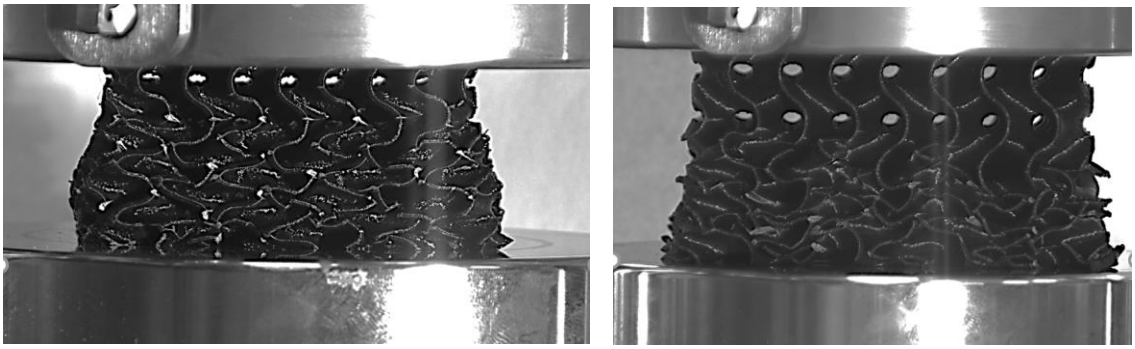

(c) (d)

Figure 17: Final deformation of samples with constant wall thickness at 50% of strain. G-4-129 (a), G-8-1.29 (b), G-12-1.29 (c), G-16-1.29 (d).

The scaffold with lowest porosity (G-4-1.29) shows a streching deformation, with a different final conformation of the compressed samples with a notable densification, while for scaffolds with higher porosity (G-16-1.29 and G-12-1.29) there are bonding deformations, where porous scaffolds are simply crushed under the compressive load by buckling of struts, in consecutive layer-by-layer failures. This different behavior confirms that scaffolds with higher value of porosity tends to deform in layer-by-layer way.

3.3) Constant porosity

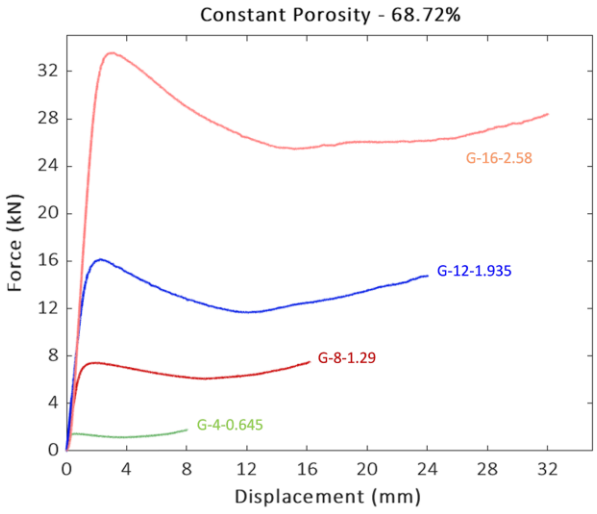

(a)

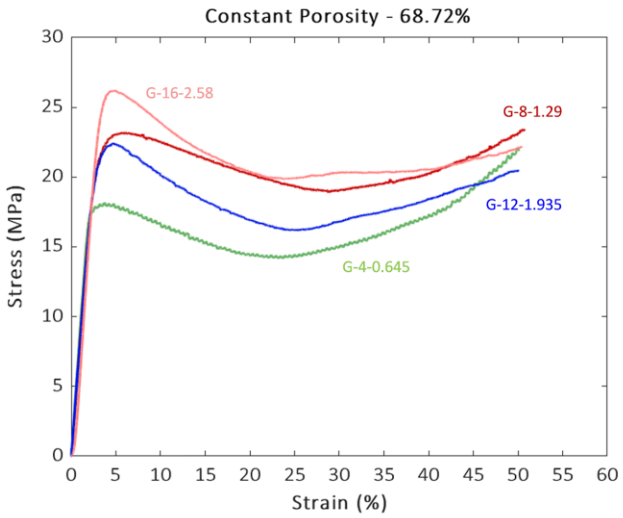

(b)

Sample	Wall thickness (mm)	Yield Strength (MPa)	Young's Modulus (MPa)
G-4-0.645	0.645	18.17	892.25
G-8-1.29	1.29	23.2	764.2
G-12-1.935	1.935	22.45	840
G-16-2.58	2.58	26.22	770.45

(c)

Figure 18: (a) Load-Displacemente curves, (b) Stress-Strain curves and (c) calculated parameters for set with constant porosity.

The porosity of trabecular (cancellous) bone can lie anywhere in the range of 30% to more than 90% and is dependent upon bone location, sex, and state of health. A porosity of 68.72% is selected for this study and is centered on values pertinent to the human pelvic and knee region. Indeed, as seen from literature, this value is a typical specification for structures suitable for application in orthopedic surgery [37].

All the stress–strain curves for all the samples show similar trend with the Yield stress and peak compressive stress that are reached at approximately 5% and a sudden rise in the load value corresponding to densification around 30% of strain. When reaching 50% of strain, all curves tend to merge on one point.

No direct or inverse relationship is present between the increase of unit cell size and Yield Strength or Young's Modulus. What is interesting is that the sample with the smallest unit cell size (4 mm) has the lowest compressive strength and stiffness. This is an important result as it indicates that from a strength point of view there is little to be gained by building constructs with unnecessarily small cells. Infact, increasing the cell size to 8mm provide a higher value of Yield Strength (23.2 MPa) compared to 4mm. This value is also higher than the lattice with 12mm unit cell size, although their values are very close. A further increasing of the unit cell size at 16mm

leads to an increase in Yield Strength and a overall cubic sample size of 64x64x64 mm. From a biomechanical point of view having such a large sample is not useful in the field of surgery. Indeed, increasing the unit cell size could have disadvantage of increasing the pore size, which might make the structure unsuitable for bone implants [38].

3.4) Energy absorption

Another interesting parameter which must be analyzed is the capacity of energy absorption of specimens under compression. Accordingly, the energy absorption per unit volume is calculated as: $SEA_v = \frac{EA}{\delta V}$ (7).

The total energy absorption is exactly the integration of the stress-strain curves under compression and the corresponding results for the three categories are plotted in Figure 19:

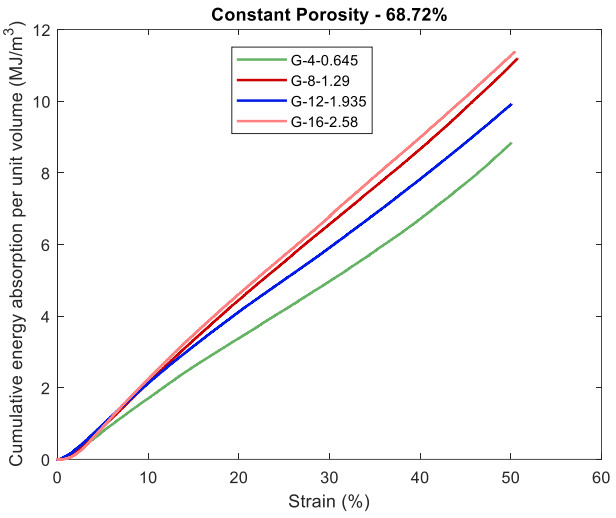

(a)

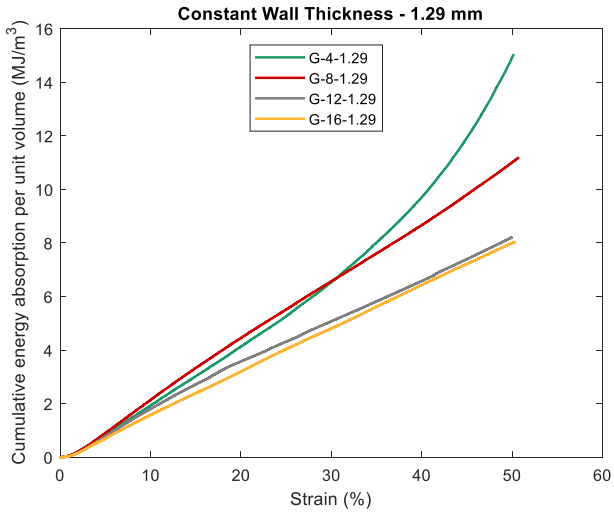

(b)

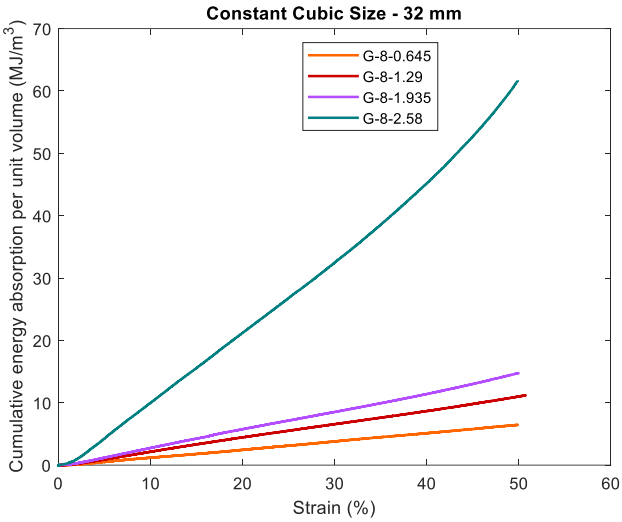

(c)

Figure 19: Energy absorption plots for the three different categories of (a) constant porosity, (b) constant wall thickness and (c) constant cubic size.

The plot with constant porosity shows that the smallest/largest unit cells and wall thickness (G-4-0.645 and G-16-2.58) have the smallest/largest energy absorption per unit volume. The plot with constant wall thickness shows that G-12-1.29 and G-16-1.29 have very similar energy absorption per unit volume vs strain curve, while G-4-1.29 shows the growth trend exponentially after 30% of strain. So that, the SEA_v are enlarged with the increasing relative density, as it can be straightforwardly understood that large relative density will enable more material to absorb the

strain energy under deformation. However, all the lattices show linear trend for cumulative energy absorption per unit volume curve within 0-50% of the strain. The plot with constant cubic size shows that G-8-2.58 has much higher cumulative energy absorption per unit volume under the same strain than the rest three curves.

Analysis presented in Figure 20 compares the influence of surface thickness and number of cells on Gyroid energy absorption per unit volume. These results indicate that:

1)when the unit cell size stays still, the energy absorption per unit volume rises with the wall thickness increases;

2)with the same wall thickness, more energy can be absorbed by porous structure if we decrease the size of the unit cell.

That behaviour is also confirmed by literature [39].

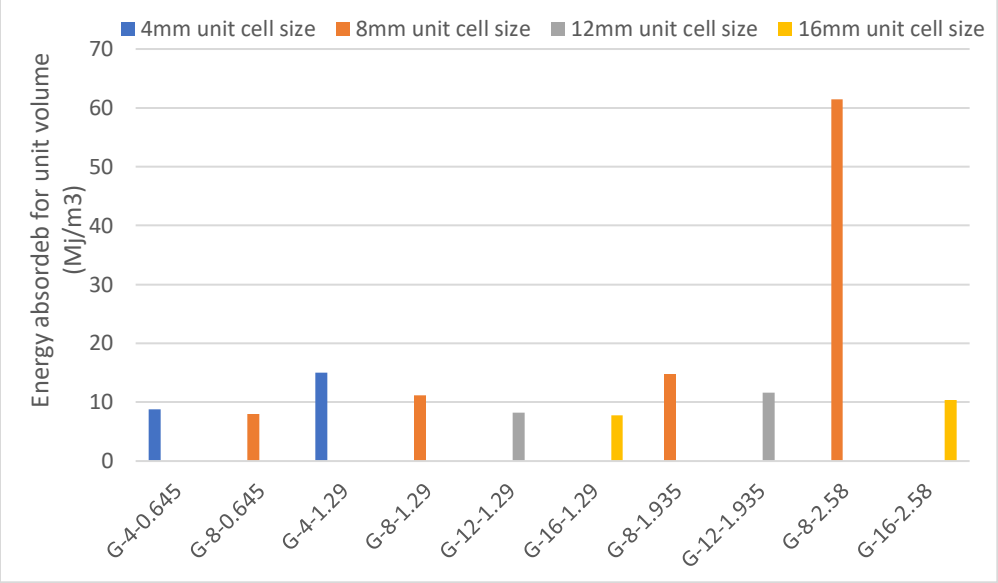

Figure 20: Comparison of energy absorption value for every single speciment.

3.5) DIC observations

The elaborated data and images resulting from DIC analysis for three specific gyroid lattice samples are showed belowe in Figure 21:

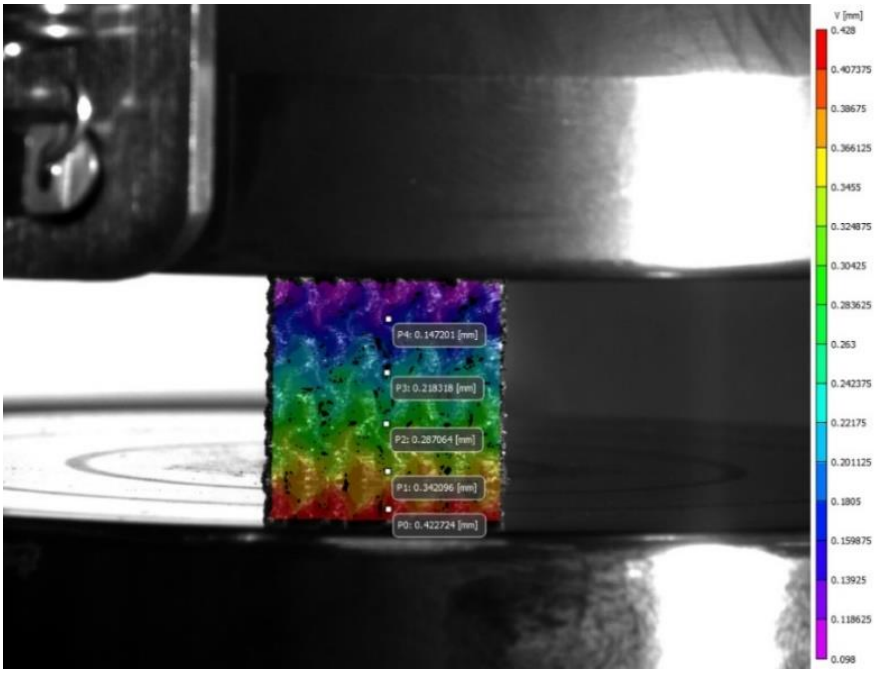
V [mm]
0.428
0.407375
0.38675
0.366125
0.3455
0.324875
0.30425
0.283625
0.263
0.242375
0.22175
0.201125
0.1805
0.159875
0.13925
0.118625
0.098
P4: 0.147201 [mm]
P3: 0.218318 [mm]
P2: 0.287064 [mm]
P1: 0.342096 [mm]
P0: 0.422724 [mm]

(a)

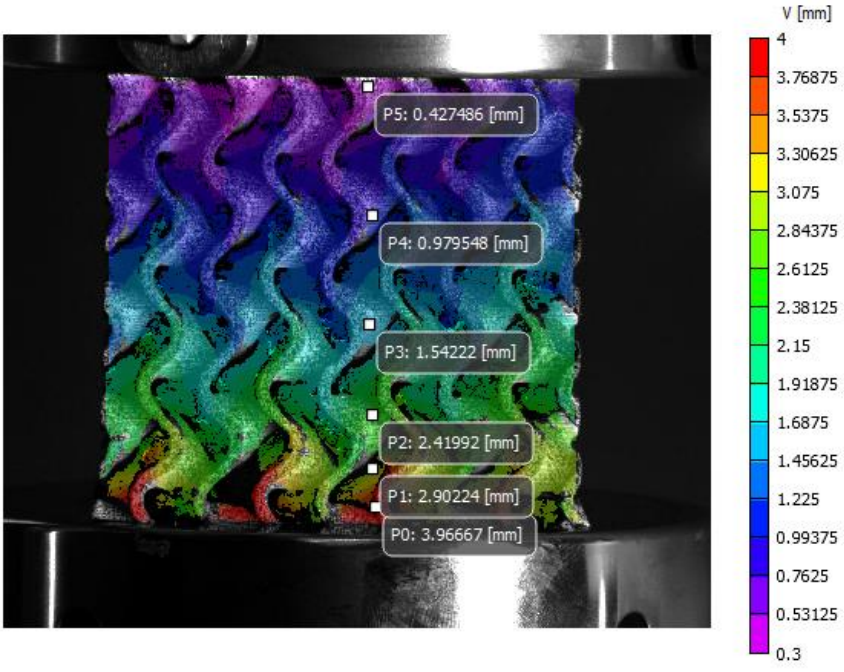
V [mm]
4
3.76875
3.5375
3.30625
3.075
2.84375
2.6125
2.38125
2.15
1.91875
1.6875
1.45625
1.225
0.99375
0.7625
0.53125
0.3
P5: 0.427486 [mm]
P4: 0.979548 [mm]
P3: 1.54222 [mm]
P2: 2.41992 [mm]
P1: 2.90224 [mm]
P0: 3.96667 [mm]

(b)

(c)

Figure 21: DIC visualization for (a) G-4-0.25, (b) G-16-2.58 and (c) G-8-1.29.

Figure 21a and Figure 21b are chosen as representative and they refer to samples G-4-0.645 and G-16-2.58, the smallest and bigger sample, respectively. As for this two scaffolds, all the gyroidal lattice structures show an orizontal propagation of displacement that suggest a layer by layer pattern failure that starts from bottom and propagates towards top. This general behavior is also confirmed in literature as shown by Khogalia et Al. [40].

The only one that shows a different result is the sample G-8-1.29. This scaffolds exhibits deformation with shear bands diagonal to the dispacement direction imposed for the compression tests, as seen in Figure 21c. This result suggests that there will be a failure of the scaffold along the shear band, resulting in separation of the same scaffold into two pieces. This behaviour is similar to the one presented by metallic scaffolds with same structural characteristic [41, 42].

3.6) Convergence between compression test and FEA

The FEA visualization results for the representative sample G-8-1.29 are presented in Figure 22:

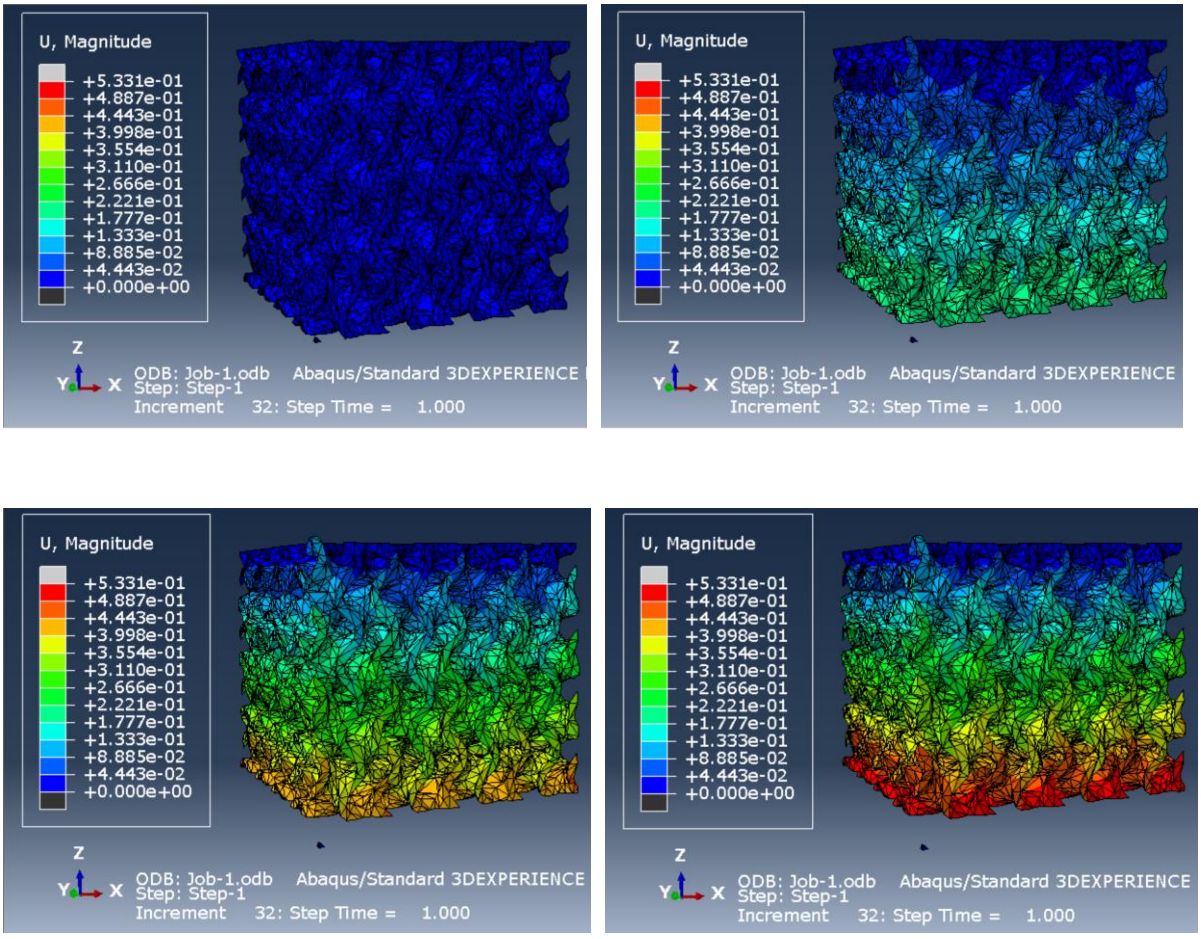

Figure 22: Abaqus representative results after the application of a displacement of 0.5mm for G-8-1.29.

The data obtained from the numerical analysis are processed to obtain the stiffness of each individual sample. These values are compared with the stiffness values obtained from the experiments and presented together in figure 23:

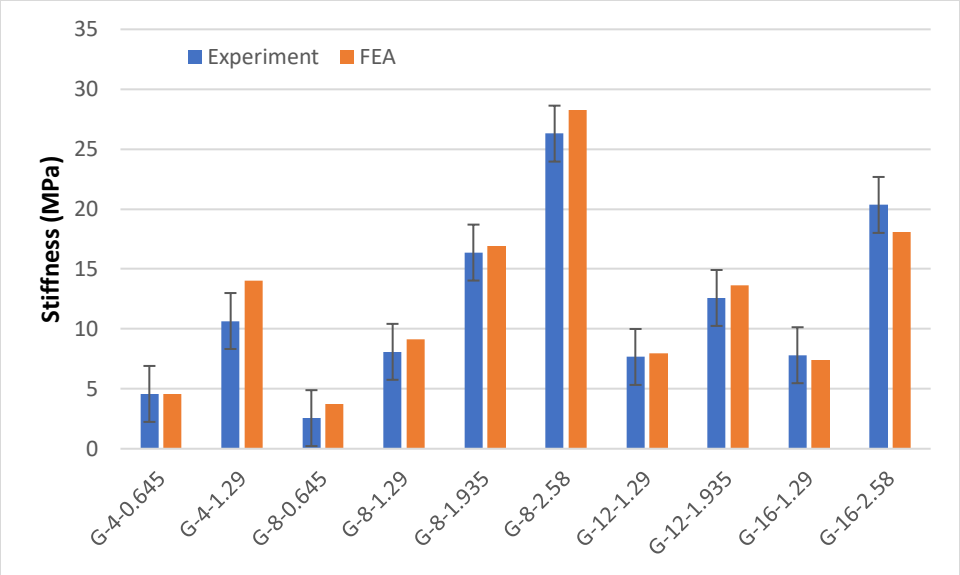
Experiment
FEA
Stiffness (MPa)
35
30
25
20
15
10
5
0
G-4-0.645
G-4-1.29
G-8-0.645
G-8-1.29
G-8-1.935
G-8-2.58
G-12-1.29
G-12-1.935
G-16-1.29
G-16-2.58

(a)

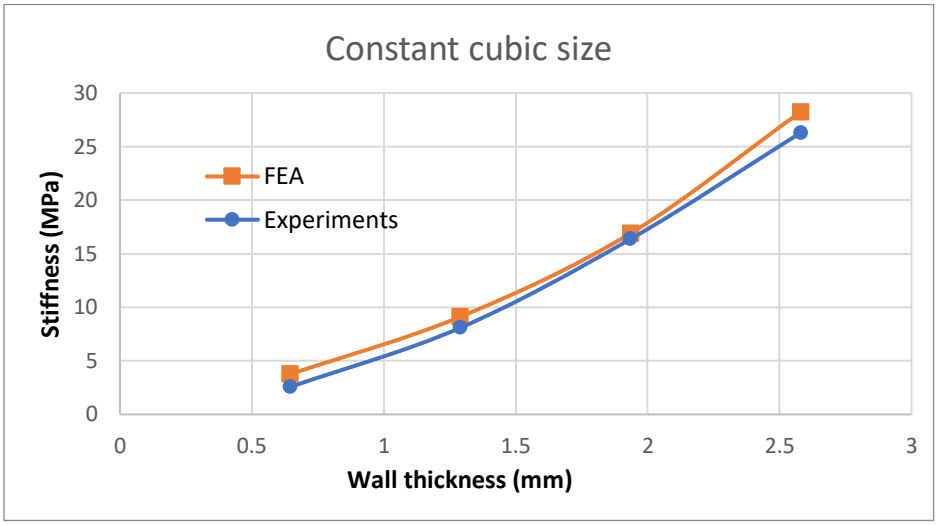
Constant cubic size
Stiffness (MPa)
30
25
20
15
10
5
0
FEA
Experiments
0
0.5
1
1.5
2
2.5
3
Wall thickness (mm)

(b)

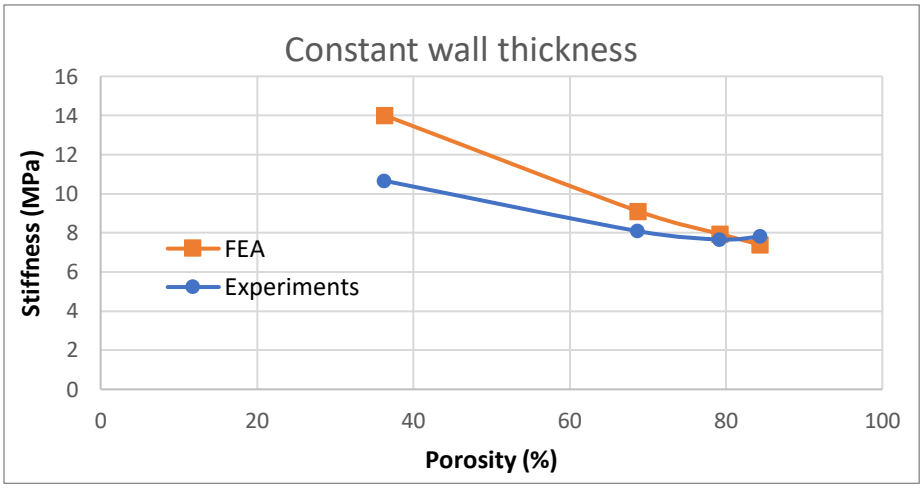
Constant wall thickness
Stiffness (MPa)
16
14
12
10
8
6
4
2
0
FEA
Experiments
0
20
40
60
80
100
Porosity (%)

(c)

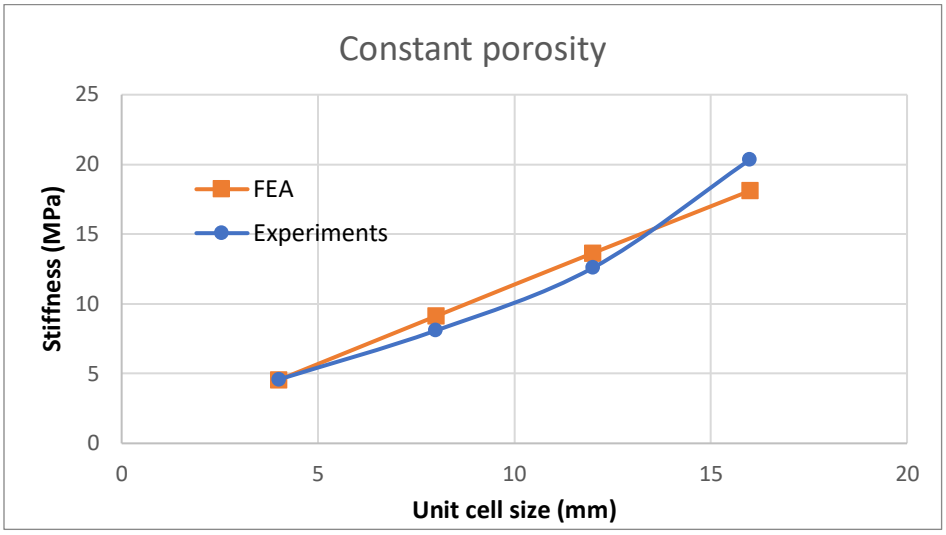

(d)

Figure 23: Comparison of stiffness values for experimental and numerical data for (a) all the samples, (b) set with constant cubic size, (c) set with constant wall thickness, and (e) set with constant porosity.

The comparison of results shows that the data obtained from the experiment are really close to the ones obtained from the Numerical Analysis. The differences of values between the experimental data and the FEA data are due to samples imperfection linked to their production, while the samples analyzed with the software are considered ideal and without defects.

This means that the FEM simulation can be a powerful tool to determine the mechanical behaviors of these type of structures, including force, deformation, stress, strain, elastic modulus, and strength in different loading regime, including compression, tension, bending, fatigue, and fracture under static and dynamic states. Moreover, other analysis as thermal and fluid mechanics can be analyzed by this method. Thus, the FEM method combined with new healthcare technologies has the potential to predict the scaffold's properties under various physiological and biomechanical conditions, as also seen in other work from literature [43].

Chapter 4: Conclusions & Future works

The mechanical properties of 3D structures are an important feature when considering the final application of the scaffolds. In particular, in that work the scale effect is studied keeping constant porosity of approximately 68.72%, the geometry effect is analyzed keeping wall thickness constant at 1.29 mm and the wall thickness effect is seeing through constant cubic size and unit cell size, 32 mm and 8 mm respectively. The influence of these diverse geometric parameters on the mechanical properties of samples has been investigated by numerical and experimental techniques and the results can be summarized as follows. Considering that this work is part of a project which intends to go on with further analysis and insights, future works are also presented.

4.1) Conclusions

- By increasing unit cell size keeping constant wall thickness, porosity increases, and volume fraction decreases. Conversely, with increasing wall thickness keeping constant cubic cell size, porosity decreases, and surface area increases. The variation of these two design parameters, and their ratio to one another, enables prescribed modulation of topological properties (porosity, surface area, interconnectivity), and thus resulting effective properties (permeability, stiffness, strength). Unit cell size nor wall thickness independently are shown to have a dominating influence; rather their ratio to one another, which controls the macroscopic porosity of the gyroid lattice, dominates mechanical properties. What can be observe is that constant wall thickness and constant cubic sizes have the largest influence on the plateau stress, Young's modulus, and energy absorption capacity, while the effect of constant porosity is much smaller, as also confirmed by literature [44]. Indeed, the Young's Modulus for samples with constant porosity is in the range of 764.2 – 892.25 MPa, while the Young's Modulus for samples with constant cubic size and constant wall thickness is 589.2 – 3893.6 MPa and 685.27 – 1051.5 MPa, respectively.

- The best mechanical properties are obtained for specimens G-8-2.58 that shows results three times higher than the other samples. G-4-1.29, G-8-1.935 and G-16-2.58 also show good mechanical values and are linked with the G-8-2.58 having same porosity, same unit cell size and same wall thickness, respectively. The poorest mechanical response is obtained by structures G-8-0.645 and G-12-1.29 that show values of porosity higher compared to the sample mentioned before. It can be supposed that avoid 0.645 mm as wall thickness, 12 mm as unit cell size and a porosity higher than or equal to 79% allows to obtain samples with more interesting mechanical responses.

- The energy absorption of samples shows that thickening the surface of the samples by multiple increments is more effective in increasing energy absorption than the addition of cells to the Gyroid topology. This analysis indicates strong potential in achieving superior mechanical properties of gyroid structure by calibrating the two factors thickness and number of cells, in order to simulate the mechanical strength and modulus of the human cortical bone, as also shown from literature for gyroidal structure made with different material [45]. Also, the energy absorption capacity of lattices G-8-2.58, with 36.31% of porosity, has the same values of the energy absorption per unit volume of a titanium foam at a porosity of 71.32% at the same point of strain (50%) [46]. This value is around 55.6 MJ/m3, which is significantly larger than values reported earlier for polymer lattice structures [47] evidencing potential for energy absorbing applications.

- All specimens showed signs of damage localization. This behavior is consistent with the mechanical response of porous materials under compression, in which deformation is associated with strain localization, typically in the form of bands, which determine the onset of yielding, hardening, and the level of plateau stress. This behavior is seen in other reports also for other materials like nickel and alumina [48, 49, 50]. The samples with the highest values of porosity (84.38% for G-8-0.645 and G-16-1.29, and 79.23% for G-12-1.29) show damage in the form of horizontal localization bands, crushed layers of cells. In those samples, the plastic collapse of the structure took place on a layer-by-layer basis, with

minimal or localized variations in its cross-section. Indeed, this type of structural failure gave rise to stress-strain curves, where the strength is repeatedly lost and recovered as each layer collapsed and is compressed into the one below. The other samples, with lower value of porosity in a range of 36.31%-68.72%, show a predominantly ductile failure which referred to the smooth transition of the compressive load within the layers of the lattice structure. In just one case, the one refers to G-8-1.29, the localization seems to take place along the diagonal of the specimen, that could lead to the fracture of the specimen due to the propagation of a cracks through the lattice as also usually seen in literature [51].

- Considering that the Elastic modulus and Yield Strength of cancellous bone stimated under compression are in the ranges of 10-1570 MPa and 1.5–38 MPa, respectively [52, 53, 54], while the Young's Modulus and Yield Strength of the studied PLA gyroid scaffolds is in a range of 589.2 – 1008.5 MPa and 14.01 – 29.1 MPa, respectively, it can be concluded that the use of these designs as trabecular bone scaffold could be considered. Two exception are made from that last consideration: the first one is for lattice G-8-2.58 which presents 3893.6 MPa as values of Young's modulus and 106.82 MPa for the Yield Strength. That value are not included in the range mentioned previously for cancellous bone; the second one is for G-16-1.29 and G-16-2.58. Both of them present a Young's modulus and Yeld Strength in the range of 750-770 MPa and 18-26 MPa respectively, but their dimensions may not be suitable for biomedical applications.

4.2) Future works

- Analysis of the same samples through Differential Scanning Calorimetry (DSC) for the detection of endothermic and exothermic transitions of the material, like the determination of transformation temperatures and enthalpy of solids as a function of temperature; capture of optical images on the samples to investigate the types of fractures more thoroughly; study the crystallinity of the material before and after samples production.

- Extension of the results of this research to other materials, for example polymers with higher or lower ductility, or metals, also produced with different AM techniques. This can lead to perform different tests and analysis which can also allow to obtain other material properties, as those studied through fatigue tests.

- Improvement of the mechanical and biological performance of these structures implementing surface modifications, as the use of different type of unit cell size, and making post manufacturing treatment on their surface, in order to reduce the possible effect of residual stress components.

Outcomes

Part of the work has been submitted to the conference "26th International Conference on Fracture and Structural Integrity" (IGF26, May 26-31, 2021, Turin (Italy) & Web). This thesis will be also part of an upcoming journal paper.

REFERENCES

[1] Ngo, T. D., Kashani, A., Imbalzano, G., Nguyen, K. T. Q., & Hui, D. (2018). *Additive manufacturing (3D printing): A review of materials, methods, applications and challenges*. Composites Part B: Engineering, 143, 172–196.

[2] Tappa, K., & Jammalamadaka, U. (2018). *Novel Biomaterials Used in Medical 3D Printing Techniques.* Journal of Functional Biomaterials, 9(1), 17.

[3] Shahrubudin, N., Lee, T. C., & Ramlan, R. (2019). *An Overview on 3D Printing Technology: Technological, Materials, and Applications.* Procedia Manufacturing, 35, 1286–1296.

[4] Poologasundarampillai, G., & Nommeots-Nomm, A. (2017). *Materials for 3D printing in medicine. 3D Printing in Medicine, 43–71.*

[5] Akhoundi, B., & Behravesh, A. H. (2019). *Effect of Filling Pattern on the Tensile and Flexural Mechanical Properties of FDM 3D Printed Products.* Experimental Mechanics.

[6] Ghomi, E. R., Khosravi, F., Neisiany, R. E., Singh, S., & Ramakrishna, S. (2020). *Future of Additive Manufacturing in Healthcare.* Current Opinion in Biomedical Engineering, 100255.

[7] Sears, N. A., Seshadri, D. R., Dhavalikar, P. S., & Cosgriff-Hernandez, E. (2016). *A Review of Three-Dimensional Printing in Tissue Engineering.* Tissue Engineering Part B: Reviews, 22(4), 298–310.

[8] Hodzic D, Pandzic A, Hajro I, Tasic P. (2020). *Strength comparison of FDM 3D printed PLA made by different manifactures.* TEM Journal, 9(3), 966-970.

[9] Thavornyutikarn, B., Chantarapanich, N., Sitthiseripratip, K., Thouas, G. A., & Chen, Q. (2014). *Bone tissue engineering scaffolding: computer-aided scaffolding techniques.* Progress in Biomaterials, 3(2-4), 61–102.

[10] Gross, B. C., Erkal, J. L., Lockwood, S. Y., Chen, C., & Spence, D. M. (2014). *Evaluation of 3D Printing and Its Potential Impact on Biotechnology and the Chemical Sciences.* Analytical Chemistry, 86(7), 3240–3253.

[11] Karim, L., Hussein, A. I., Morgan, E. F., & Bouxsein, M. L. (2013). *The Mechanical Behavior of Bone.* Osteoporosis, 431–452.

[12] Ifeanyichukwu E., Xiaobing F., Ben D., Richard L., Samanta P. (2019). *Review of defects in lattice structures manufactured by powder bed fusion*. The International Journal of Advanced Manufacturing Technology.

[13] Ronca, A., Rollo, G., Cerruti, P., Fei, G., Gan, X., Buonocore, G., … Ambrosio, L. (2019). *Selective Laser Sintering Fabricated Thermoplastic Polyurethane/Graphene Cellular Structures with Tailorable Properties and High Strain Sensitivity.* Applied Sciences, 9(5), 864.

[14] Hao P., Feng G., Wenjing H. (2019). *Design, modeling and characterization of triply periodic minimal surface heat exchangers with additive manufacturing.* Proceedings of the 30th Annual International Solid Freeform Fabrication Symposium – An Additive Manufacturing Conference.

[15] Kapfer, S. C., Hyde, S. T., Mecke, K., Arns, C. H., & Schröder-Turk, G. E. (2011). *Minimal surface scaffold designs for tissue engineering.* Biomaterials, 32(29), 6875–6882.

[16] Al-Ketan, O., Rowshan, R., & Abu Al-Rub, R. K. (2018). *Topology-mechanical property relationship of 3D printed strut, skeletal, and sheet based periodic metallic cellular materials.* Additive Manufacturing, 19, 167–183.

[17] Yuan, L., Ding, S., & Wen, C. (2019). *Additive manufacturing technology for porous metal implant applications and triple minimal surface structures: A review*. Bioactive Materials, 4(1), 56–70.

[18] Benedetti M., Du Plessis A, Ritchie R.O., Dallago M., Razavi S.M.J., Berto F. (2021). *Architected cellular materials: A review on their mechanical properties towards fatigue-tolerant design and fabrication.* Materials Science and Engineering: R: Reports.

[19] Fantini, M., Curto, M., & De Crescenzio, F. (2016). *TPMS for interactive modelling of trabecular scaffolds for Bone Tissue Engineering.* Advances on Mechanics, Design Engineering and Manufacturing, 425–435.

[20] Kumar, A., Nune, K. C., Murr, L. E., & Misra, R. D. K. (2016). *Biocompatibility and mechanical behaviour of three-dimensional scaffolds for biomedical devices: process–structure–property paradigm.* International Materials Reviews, 61(1), 20–45.

[21] Rho, J.-Y., Kuhn-Spearing, L., & Zioupos, P. (1998). *Mechanical properties and the hierarchical structure of bone.* Medical Engineering & Physics, 20(2), 92–102.

[22] Wang, X., Xu, S., Zhou, S., Xu, W., Leary, M., Choong, P., … Xie, Y. M. (2016). *Topological design and additive manufacturing of porous metals for bone scaffolds and orthopaedic implants: A review.* Biomaterials, 83, 127–141.

[23] Henkel, J., Woodruff, M. A., Epari, D. R., Steck, R., Glatt, V., Dickinson, I. C., … Hutmacher, D. W. (2013). *Bone Regeneration Based on Tissue Engineering Conceptions — A 21st Century Perspective.* Bone Research, 1(3), 216–248.

[24] B. Substitutes, N. A. Nawawi, A. S. F. Alqap, and I. Sopyan. (2011). *Recent Progress on Hydroxyapatite-Based Dense Biomaterials for Load Bearing Recent Progress on Hydroxyapatite-Based Dense Biomaterials for Load Bearing Bone Substitutes.*

[25] Tang Mei Shick, Aini Zuhra Abdul Kadir , Nor Hasrul Akhmal Ngadiman and Azanizawati Ma'aram (2019). *A review of biomaterials scaffold fabrication in additive manufacturing for tissue engineering.* Journal of Biomedical and Compatible Polymers, 1-21.

[26] Ahmadreza H., Fort W., Suleiman A. (2020). *Digital image correlation and its application in an undergraduate Civil Engineering Materials Laboratory.*

[27] Vanderesse, N., Richter, A., Nuño, N., & Bocher, P. (2018). *Measurement of deformation heterogeneities in additive manufactured lattice materials by Digital Image Correlation: Strain maps analysis and reliability assessment*. Journal of the Mechanical Behavior of Biomedical Materials, 86, 397–408.

[28] P. Pawar, R., U. Tekale, S., U. Shisodia, S., T. Totre, J., & J. Domb, A. (2014). *Biomedical Applications of Poly(Lactic Acid).* Recent Patents on Regenerative Medicine, 4(1), 40–51.

[29] Singhvi, M. S., Zinjarde, S. S., & Gokhale, D. V. (2019). *Poly-Lactic acid (PLA): synthesis and biomedical applications.* Journal of Applied Microbiology.

[30] Vigneshwaran S., Oisik D., Karthik B., Uthayakumar M., Arumugaprabu V., Deepak J.J., Rasoul E. N., Mikael S., Seeram R., Filippo B. (2020). *Fatigue behaviour of FDM-3D printed polymers, polymeric composites and architected cellular materials.* International Journal of Fatigue.

[31] Kelly, C. N., Francovich, J., Julmi, S., Safranski, D., Guldberg, R. E., Maier, H. J., & Gall, K. (2019). *Fatigue Behavior of As-Built Selective Laser Melted Titanium Scaffolds with Sheet-based Gyroid Microarchitecture for Bone Tissue Engineering.* Acta Biomaterialia.

[32] Alizadeh-Osgouei, M., Li, Y., Vahid, A., Ataee, A., & Wen, C. (2020). *High strength porous PLA gyroid scaffolds manufactured via fused deposition modeling for tissue-engineering applications.* Smart Materials in Medicine.

[33] Harshit K. Dave, Shilpesh R. Rajpurohit, Naushil H. Patadiya, Shalin J. Dave, Kumar S. Sharma, Siddharth S. Thambad, Varunkumar P. Srinivasn, Khyati V. Sheth. *Compressive strength of PLA based scaffolds: effect of layer height, infill density and print speed.* International Journal of Modern Manufacturing Technologies.

[34] Abueidda, D. W., Bakir, M., Abu Al-Rub, R. K., Bergström, J. S., Sobh, N. A., & Jasiuk, I. (2017). *Mechanical properties of 3D printed polymeric cellular materials with triply periodic minimal surface architectures.* Materials & Design, 122, 255–267.

[35] Maharjan, G. K., Khan, S. Z., Riza, S. H., & Masood, S. (2018). *Compressive Behaviour of 3D Printed Polymeric Gyroid Cellular Lattice Structure.* IOP Conference Series: Materials Science and Engineering, 455, 012047).

[36] Tripathi, Y., Shukla, M., & Bhatt, A. D. (2019). *Implicit-Function-Based Design and Additive Manufacturing of Triply Periodic Minimal Surfaces Scaffolds for Bone Tissue Engineering.* Journal of Materials Engineering and Performance.

[37] Mullen, L., Stamp, R. C., Brooks, W. K., Jones, E., & Sutcliffe, C. J. (2009). *Selective Laser Melting: A regular unit cell approach for the manufacture of porous, titanium, bone in-growth constructs,*

suitable for orthopedic applications. Journal of Biomedical Materials Research Part B: Applied Biomaterials, 89B(2), 325–334.

[38] Du Plessis, A., Yadroitsava, I., Yadroitsev, I., le Roux, S., & Blaine, D. (2018). *Numerical comparison of lattice unit cell designs for medical implants by additive manufacturing.* Virtual and Physical Prototyping, 13(4), 266–281.

[39] Hailiang W., David Z., Peng Z., Zhihao R. (2017). *The research of compression and energy absorption property of Ti6Al4V porous structure based on selective laser melting.* Advances in Engineering Research, volume 134.

[40] Khogalia, E. H., Choo, H. L., & Yap, W. H. (2020). *Performance of triply periodic minimal surface lattice structures under compressive loading for tissue engineering applications.* 13th international engineering research conference.

[41] Anh P., Cambre K., Ken G., (2020). *Free boundary effects and representative volume elements in 3D printed Ti-6Al-4V gyroid structures.* Journal of Materials Research.

[42] Bobbert, F. S. L., Lietaert, K., Eftekhari, A. A., Pouran, B., Ahmadi, S. M., Weinans, H., & Zadpoor, A. A. (2017). *Additively manufactured metallic porous biomaterials based on minimal surfaces: A unique combination of topological, mechanical, and mass transport properties.* Acta Biomaterialia, 53, 572–584.

[43] Soufivand, A. A., Abolfathi, N., Hashemi, S. A., & Lee, S. J. (2020). *Prediction of mechanical behavior of 3D bioprinted tissue-engineered scaffolds using finite element method (FEM) analysis.* Additive Manufacturing, 101181.

[44] Rafael G. S., Cristobal S. E., Gustavo M. P., Jorge Z. V., Maria J.T. (2021). *Influence of Geometric and Manufacturing Parameters on the Compressive Behavior of 3D Printed Polymer Lattice Structures.* Additive Manufacturing Methods and Modeling Approaches.

[45] Eric Y., Martin L., Bill L., David D., Maciej M., Avik S., AmirMahyar K., f, Alistair J., Tobias M., Stuart B., Mark E., Ma Q., Peter C., Milan B. (2019). *Effect of geometry on the mechanical properties of Ti-6Al-4V Gyroid structures fabricated via SLM: A numerical study.* Material and Design.

[46] Xie, B., Fan, Y. Z., Mu, T. Z., & Deng, B. (2017). *Fabrication and energy absorption properties of titanium foam with CaCl 2 as a space holder.* Materials Science and Engineering: A, 708, 419–423.

[47] Rossiter, J.D.; Johnson, A.A.; Bingham, G.A. (2020). *Assessing the Design and Compressive Performance of Material Extruded Lattice Structures. 3D Print. Addit. Manuf.* 7, 19–27.

[48] Badiche, X., Forest, S., Guibert, T., Bienvenu, Y., Bartout, J.-D., Ienny, P., … Bernet, H. (2000). *Mechanical properties and non-homogeneous deformation of open-cell nickel foams: application of the mechanics of cellular solids and of porous materials.* Materials Science and Engineering: A, 289(1-2), 276–288.

[49] ISSEN, K., CASEY, T., DIXON, D., RICHARDS, M., & INGRAHAM, J. (2005). *Characterization and modeling of localized compaction in aluminum foam.* Scripta Materialia, 52(9), 911–915.

[50] Mu, Y., Yao, G., Liang, L., Luo, H., & Zu, G. (2010). *Deformation mechanisms of closed-cell aluminum foam in compression.* Scripta Materialia, 63(6), 629–632.

[51] Maskery, I., Aboulkhair, N. T., Aremu, A. O., Tuck, C. J., & Ashcroft, I. A. (2017). *Compressive failure modes and energy absorption in additively manufactured double gyroid lattices.* Additive Manufacturing, 16, 24–29.

[52] S.N.Khan, R. M. Warkhedkar, A.K.Shyam. (2014). *Human Bone strength Evaluation through different Mechanical Tests.* International Journal of Current Engineering and Technology.

[53] Goldstein, S. A. (1987). *The mechanical properties of trabecular bone: Dependence on anatomic location and function.* Journal of Biomechanics, 20(11-12), 1055–1061.

[54] Kokot, G., Makuch, A., Skalski, K., & Bańczerowski, J. (2018). *Mechanical properties of cancellous tissue in compression test and nanoindentation.* Bio-Medical Materials and Engineering, 29(4), 415–426.